



# Structure of Synthetic K-rich Birnessites Obtained by HighTemperature Decomposition of $\text{KMnO}_4$ . 2 Phase and Structural Heterogeneities

Anne-Claire Gaillot, Victor.A. Drits, Alain Plançon, Bruno Lanson

## ► To cite this version:

Anne-Claire Gaillot, Victor.A. Drits, Alain Plançon, Bruno Lanson. Structure of Synthetic K-rich Birnessites Obtained by HighTemperature Decomposition of  $\text{KMnO}_4$ . 2 Phase and Structural Heterogeneities. Chemistry of Materials, American Chemical Society, 2004, 16, pp.1890-1905. <10.1021/cm035236r>. <hal-00193734>

**HAL Id: hal-00193734**

**<https://hal.archives-ouvertes.fr/hal-00193734>**

Submitted on 4 Dec 2007

**HAL** is a multi-disciplinary open access archive for the deposit and dissemination of scientific research documents, whether they are published or not. The documents may come from teaching and research institutions in France or abroad, or from public or private research centers.

L'archive ouverte pluridisciplinaire **HAL**, est destinée au dépôt et à la diffusion de documents scientifiques de niveau recherche, publiés ou non, émanant des établissements d'enseignement et de recherche français ou étrangers, des laboratoires publics ou privés.

**Structure of Synthetic K-rich Birnessites Obtained by High-  
Temperature Decomposition of  $\text{KMnO}_4$ .**

**III. Phase and Structural Heterogeneities**

**Anne-Claire Gaillot<sup>1</sup>**

**Victor A. Drits<sup>1,2</sup>**

**Alain Plançon<sup>3</sup>**

**Bruno Lanson<sup>1, \*</sup>**

1 – Environmental Geochemistry Group, LGIT – Maison des Géosciences, University of  
Grenoble – CNRS, 38041 Grenoble Cedex 9, France.

2 – Geological Institute, Russian Academy of Sciences, 7 Pyzhevsky street, 109017  
Moscow, Russia.

3 – Crystallography Laboratory, ISTO, University of Orléans - CNRS, 45067 Orléans  
Cedex 2, France.

\* Author to whom correspondence should be addressed.

e-mail : [Bruno.Lanson@obs.ujf-grenoble.fr](mailto: Bruno.Lanson@obs.ujf-grenoble.fr)

## Abstract

Synthetic K-rich birnessites (KBi) were prepared from the thermal decomposition of a fine-grained  $\text{KMnO}_4$  powder heated in air atmosphere at temperatures ranging from 200-1000°C. The qualitative analysis of powder X-ray diffraction (XRD) patterns reveals a complex range of structural transformations from one metastable phase to the other, often through intermediate mixed-layer structures (MLSs). Phase and structural heterogeneities of KBi samples synthesized at 700°C, 800°C and 1000°C (referred to as  $\text{KBi}_7$ ,  $\text{KBi}_{8h}$  and  $\text{KBi}_{10h}$ ) have been studied in details by chemical and thermal analysis and by simulation of the experimental powder XRD patterns. Two-layer orthogonal ( $2O$ ), and hexagonal ( $2H$ ) as well as three-layer rhombohedral ( $3R$ ) polytypes were identified in these samples. The  $2O$  structure consists of vacancy-free layers and their orthogonal symmetry is linked to the high content of layer  $\text{Mn}^{3+}$  cations and to the unique azimuthal orientation of  $\text{Mn}^{3+}$  octahedra which are elongated because of Jahn-Teller distortion. In the  $2H$  and  $3R$  polytypes, the layers have a hexagonal symmetry as they contain only  $\text{Mn}^{4+}$ - and vacant octahedra. As a result, their interlayers have a heterogeneous cation composition, because of the migration of  $\text{Mn}^{3+}$  from the layers to the interlayers. In addition to the periodic KBi polytypes,  $\text{KBi}_7$  and  $\text{KBi}_{8h}$  contain MLSs in which layer pairs of the  $2H$  polytype are interstratified at random with those of the  $3R$  or of the  $2O$  polytype. Interstratification of incommensurate  $2O$  and  $2H$  structural fragments leads to peculiar diffraction effects and represents a new type of structural disorder in birnessites. The increase of temperature from 700°C to 1000°C is associated with the replacement of  $3R/2H$ ,  $2H$ , and  $2O/2H$  mixed-layered structures by the more stable  $2O$  polytype.  $\text{KBi}_{10h}$  consists of a mixture of a minor  $2H$  phase with three  $2O$  varieties having slightly different layer unit-cell parameters. This phase heterogeneity results from the partial disorder in the orientation of  $\text{Mn}^{3+}$  octahedra. The average structural formulae,  $\text{K}^{+}_{0.265}\text{Mn}^{3+}_{0.145}(\text{Mn}^{4+}_{0.825}\square_{0.175})\text{O}_2 \cdot 0.68 \text{H}_2\text{O}$  for  $\text{KBi}_7$  and  $\text{KBi}_{8h}$ , and

$\text{K}^{+}_{0.27}(\text{Mn}^{4+}_{0.77}\text{Mn}^{3+}_{0.21}\square_{0.02})\text{O}_2 \cdot 0.53 \text{H}_2\text{O}$  for KBi<sub>10h</sub>, are in agreement with the main crystal chemical features of the phases prevailing in these samples. When heated to 350°C, the 2O polytype presents a hexagonal layer symmetry with a *b* parameter (2.894 Å) which is significantly increased as compared to that determined at room temperature (2.850 Å). Both modifications arise from random orientation of elongated Mn<sup>3+</sup> octahedra along directions forming n60° angles with the *a* axis. The main factors responsible for the phase and structural heterogeneity of the KBi samples are discussed.

## Introduction

Layers building up hydrous manganese oxides such as birnessite consist of edge-sharing MnO<sub>6</sub> octahedra. Hydrated exchangeable cations are present in the interlayer space to compensate for the layer charge deficit arising from the presence within layers of Mn<sup>3+</sup> cations and/or of vacant layer octahedra.<sup>1-6</sup> Birnessite is easily synthesized under laboratory conditions and some of the synthetic birnessite species have commonly been used as analogs of the natural species to determine the structural mechanism of heavy metal sorption or to investigate the structural modification of birnessite as a function of pH (e.g.).<sup>5-16</sup> Simultaneously, synthetic birnessites have drawn a special attention as a potential cathode material for secondary batteries following their intercalation with lithium cations.<sup>17-21</sup> Because of its apparent lamellar framework stability, K-rich birnessite (hereafter referred to as KBi) represents a promising candidate as lithium battery cathode material. This birnessite variety can be obtained from the thermal decomposition of KMnO<sub>4</sub>,<sup>21</sup> or of a mixture of MnO, KNO<sub>3</sub> and LiOH,<sup>22</sup> or from the Mn<sup>7+</sup> reduction under hydrothermal conditions.<sup>19,20</sup>

Because of their influence on reactivity it is essential to have a detailed understanding of the structural and chemical features of these birnessite species. However, structural studies of birnessite are most often impaired as these compounds occur normally in a finely dispersed

state. In addition, structural variety of birnessite is extreme as these species may differ from each other by their layer symmetry, their layer stacking, or the content and distribution of heterovalent Mn cations and layer vacancies within layers (e.g.). Furthermore, structural and chemical defects, such as the interstratification of different layer types and stacking faults, are frequent in these compounds.<sup>23</sup> As a result, only a few publications were devoted to the structural study of KBi varieties. According to Chen et al.<sup>19</sup> KBi variety synthesized under hydrothermal conditions presents a three-layer rhombohedral (3R) structure in which octahedral layers are shifted with respect to each other by  $-a/3$  (assuming an orthogonal base-centered unit cell) leading to the prismatic coordination of interlayer K coordinated to layer oxygen atoms ( $O_{\text{layer}}$ ). Kim et al.<sup>21,22</sup> synthesized new high temperature KBi and K-Li birnessite-like varieties with a two-layer polytype, in which adjacent layers are rotated with respect to each other by  $180^\circ$  around the  $c$  axis passing through the layer Mn ( $Mn_{\text{layer}}$ ) cations. Even though the main idealized structural and chemical properties of high temperature KBi have been determined,<sup>21</sup> crystal chemistry of this new polytype and significant details of its structure remain poorly understood.

In the two companion articles<sup>24,25</sup> it is shown that KBi obtained from thermal decomposition of  $KMnO_4$  at  $800^\circ\text{C}$  and  $1000^\circ\text{C}$  have different unit cells and supercells, different sources of the layer charge deficit and specific distribution of heterovalent Mn cations. However, the two KBi samples described in these articles<sup>24,25</sup> have a high structural perfection and do not contain ( $KBi_{100}$ ) or contain only a few stacking faults ( $KBi_{80}$ ). In contrast, the present article deals with phase, structural and chemical heterogeneity of KBi varieties obtained at different temperatures and assesses the origin of such variability. Specific structural and chemical heterogeneities are described for KBi and the original methodology used to reveal these structural defects is detailed.

## Main Structural Features of KBi<sub>80</sub> and KBi<sub>100</sub>

KBi samples with a high degree of structural order were obtained from thermal decomposition of KMnO<sub>4</sub> at 800°C (KBi<sub>80</sub>) and 1000°C (KBi<sub>100</sub>) and their structure refined from a single crystal<sup>24</sup> (KBi<sub>80</sub>) or using the Rietveld method on a powder XRD pattern (KBi<sub>100</sub>).<sup>25</sup> As the present description of KBi structures relies for a large part on the structures refined on these two samples, the main features of the refined models will be summarized.

Both samples have a two-layer unit cell in which adjacent layers are rotated with respect to each other by 180° around the *c* axis passing through the Mn<sub>layer</sub> cations. As a result of this specific layer stacking mode, O<sub>layer</sub> atoms from adjacent layers define in the interlayer region prismatic cavities located above or below empty tridentate cavities, sharing three edges with neighboring Mn<sub>layer</sub> octahedra (TE sites).

However, extensive differences exist between the structure models refined for samples KBi<sub>80</sub> and KBi<sub>100</sub>. The unit cell of sample KBi<sub>80</sub> is hexagonal with  $a = 2.840(1) \text{ \AA}$ , and  $c = 14.03(1) \text{ \AA}$ , and space group  $P6_3/mmc$ . The hexagonal symmetry of the layer results from the sole presence of Mn<sup>4+</sup> in the octahedral layers, the presence of 0.12 vacant layer sites per octahedron being responsible for the layer charge deficit.<sup>24</sup> This layer charge deficit is compensated for 1) by the presence of 0.08 interlayer Mn<sup>3+</sup> above or below vacant layer octahedra sharing three O<sub>layer</sub> with neighboring Mn<sub>layer</sub> octahedra to form a triple-corner surface complex (<sup>VI</sup>TC sites), and 2) by the presence of 0.24 interlayer K<sup>+</sup> in prismatic cavities located above or below empty tridentate cavities, sharing three edges with neighboring Mn<sub>layer</sub> octahedra (<sup>VI</sup>TE sites).

Contrastingly, the amount of Mn<sup>3+</sup> cations is much higher in the structure of KBi<sub>100</sub> (0.25 Mn<sup>3+</sup> per octahedron) than in that of KBi<sub>80</sub> (0.08 Mn<sup>3+</sup> per octahedron). The systematic presence of these cations in the octahedral sites of vacancy-free layers accounts for the layer charge deficit, which is compensated by the sole presence of interlayer K<sup>+</sup> cations.<sup>25</sup> To

minimize steric strains within the octahedral layers of  $\text{KBi}_{10\text{o}}$ , heterovalent  $\text{Mn}_{\text{layer}}$  cations are segregated in  $\text{Mn}^{3+}$ - and  $\text{Mn}^{4+}$ -rich rows parallel to  $[010]$ , and all  $\text{Mn}^{3+}$ -octahedra, which are elongated because of Jahn-Teller distortion, present a unique azimuthal orientation. These two features lead to the departure from the hexagonal layer symmetry, the unit cell of sample  $\text{KBi}_{10\text{o}}$  being orthogonal with  $a = 5.155 \text{ \AA}$ ,  $b = 2.846 \text{ \AA}$ ,  $c = 14.09 \text{ \AA}$ , and space group  $Cmcm$ . In addition, the regular alternation along the  $a$  axis of each  $\text{Mn}^{3+}$ -rich row with two  $\text{Mn}^{4+}$ -rows, emphasized by the associated distribution of interlayer cations, gives rise to a supercell with  $A = 3a$ .

## Experimental

$\text{KBi}$  samples were prepared from the thermal decomposition of fine-grained  $\text{KMnO}_4$  powder (particle size  $< 50 \text{ }\mu\text{m}$ ) in air following the modified procedure of Kim et al.<sup>21</sup> In the companion papers<sup>24,25</sup> a flat crucible covered by a thin layer of  $\text{KMnO}_4$  powder ( $100\text{--}180\text{mg/cm}^2$ ) was used for the pyrolysis to form homogeneous and highly periodic structures. In the present article high-temperature ( $800\text{--}1000^\circ\text{C}$ ) pyrolysis were performed with crucibles containing a thick layer of  $\text{KMnO}_4$  (Table 1). At lower temperature ( $200\text{--}700^\circ\text{C}$ ), pyrolysis was performed using a flat crucible covered by a thin layer of  $\text{KMnO}_4$  (Table 1). Heterogeneous  $\text{KBi}$  samples synthesized at  $200^\circ\text{C}$ ,  $400^\circ\text{C}$ ,  $600^\circ\text{C}$ ,  $700^\circ\text{C}$ ,  $800^\circ\text{C}$  and  $1000^\circ\text{C}$  for the present study will hereafter be referred to as  $\text{KBi}_2$ ,  $\text{KBi}_4$ ,  $\text{KBi}_6$ ,  $\text{KBi}_7$ ,  $\text{KBi}_{8\text{h}}$ , and  $\text{KBi}_{10\text{h}}$ . Details on the processing of pyrolysis products, as well as on the thermal and chemical analyses are given by Gaillot et al.<sup>24</sup>

The mean oxidation degree of manganese in birnessite was determined by potentiometric titration using  $(\text{NH}_4)_2\text{Fe}(\text{SO}_4)$  Mohr salt and sodium pyrophosphate.<sup>26,27</sup> Knowing the mean oxidation state,  $2x$ , and the atomic K/Mn ratio determined by ICP,  $y$ , it is

possible to calculate an average structural formula for a given KBi sample using the following equation<sup>24</sup>:

$$\text{K}^{+}_{2y/w}(\text{Mn}^{4+}_{(4x-6)/w}\text{Mn}^{3+}_{(8-4x)/w}\square_{1-2/w})\text{O}_2 \quad (1)$$

where  $w = (2x + y) / 2$ .

The amount of interlayer water may be introduced in this structural formula using the DTA and DTG data.

Powder XRD patterns were recorded using a Bruker D5000 powder diffractometer equipped with a Kevex Si(Li) solid detector and  $\text{CuK}\alpha_{1+2}$  radiation. Intensities were recorded from 5 to 90° at a 0.04° 2 $\theta$  interval using a 40 sec counting time per step. Full widths at half maximum intensity (FWHM) were determined for diffraction maxima using the standard EVA program available from Bruker. A rotating sample holder was used for room temperature data collections to minimize preferential orientation effects. A TTK450 Anton Paar chamber was used to record XRD patterns from samples heated *in situ*.

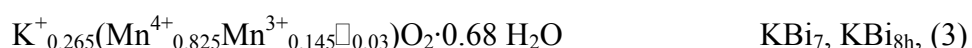
**Simulation of Powder XRD Patterns.** In the present study, samples with both high phase heterogeneity and high proportion of structural defects have been investigated. As compared to the KBi<sub>80</sub> and KBi<sub>100</sub> samples described in the two companion papers<sup>24,25</sup> the combination of these two intrinsic features impairs the ability to find a suitable single crystal and would dramatically reduce the representativeness of this crystal. These features also strongly reduce the efficiency of usual structure refinement methods including the Rietveld method. One of the most effective ways to determine the actual structure of defective layered compounds is the calculation of XRD patterns using the mathematical formalism described in detail by Drits and Tchoubar.<sup>23</sup> This trial-and-error procedure has been used successfully to determine the crystal-chemical structure of different natural and synthetic birnessites consisting of commensurate layers in the *ab* plane.<sup>12-16,28</sup> Details on the program used to calculate XRD patterns, and on the fitting procedure are given by Plançon<sup>29</sup> and Drits et al.,<sup>13</sup>



respectively. For birnessites in which partially incommensurate layers are interstratified, the mathematical formalism described by Plançon<sup>29</sup> was used. The fit quality was estimated over the 34°-56° 2θ CuKα range using the usual R<sub>wp</sub> parameter. XRD patterns calculations were restricted to 20ℓ and 11ℓ reflections (indexing based on an orthogonal base-centered unit cell) because these lines are most sensitive to structural parameters of layered minerals, including order/disorder and stacking sequences.<sup>30</sup> For each sample, the background was assumed to be linearly decreasing over the considered angular range, and preferred orientation of particles was considered as a variable parameter.

## Results

**Structural Formulae of KBi Samples.** K/Mn atomic ratios determined for KBi<sub>7</sub>, KBi<sub>8h</sub> and KBi<sub>10h</sub> are similar (0.270, 0.274 and 0.271, respectively) whereas the mean oxidation degree of Mn is lower for KBi<sub>10h</sub> (3.78) than for KBi<sub>7</sub> and KBi<sub>8h</sub> (3.87 and 3.85 – Table 2). From these analytical results, and the experimentally determined structural water weight losses (Table 2) the following formulae may be deduced from Equation (1):



**Main Features of the Experimental Powder XRD Patterns.** XRD patterns collected for KBi samples synthesized at temperatures ranging 200-1000°C all exhibit basal reflections at ~7.13 Å and ~3.56 Å characteristic of the layered structure of birnessite (Figure 1). However, the profiles of these basal reflections, as well as the number, the position, the FWHM, the profiles and the relative intensities of *hkl* reflections differ significantly from one pattern to the other (Figure 1). These differences are indicative of the structure contrast between the different samples. For example, KBi<sub>2</sub> possesses a turbostratic structure as its

XRD pattern contains only basal reflections and un-modulated two-dimensional 20,11 and 31,02 diffraction bands. KBi<sub>4</sub> also has very a low degree of structural order as its XRD pattern only contains, in addition to 20,11 and 31,02 diffraction bands, two very broad modulations at 37.3 and 42.1°2θ CuKα (2.410 and 2.145 Å, respectively). From 600°C and up, XRD patterns of KBi samples exhibit well-defined, sharp and intense *hkl* reflections whose position shifts and intensity distribution modifications reflect the evolution of the KBi structure as a function of synthesis temperature. Structural and crystal-chemical features of KBi samples synthesized at 700-1000°C will be detailed below. To differentiate the homogeneous samples obtained at 800° and 1000°C and described by Gaillot et al. from the heterogeneous KBi<sub>10h</sub> and KBi<sub>8h</sub> samples described in the present paper, the former ones will hereafter be referred to as KBi<sub>10o</sub> and KBi<sub>8o</sub>.<sup>24,25</sup>

**Indexation of the Experimental Powder XRD Patterns.** All XRD patterns were indexed using base-centered orthogonal unit cells independently of their hexagonal ( $a = b\sqrt{3}$ ) or orthogonal ( $a > b\sqrt{3}$ ) layer symmetry. Therefore, reflections located in the 34°-70° 2θ CuKα range have 20 $\ell$ ,11 $\ell$  indices and 31 $\ell$ ,02 $\ell$  ones in the 64°-70° 2θ CuKα range.

*KBi<sub>10h</sub>*. In the 34°-56° 2θ range, two sets of non-basal reflections may be distinguished (Figures 1, 2). The first one consists of intense and sharp reflections (2.485, 2.347, 2.204, 2.040, 1.718 Å) which can be indexed using a hexagonal two-layer (2H) unit cell, with  $a = 4.976$  Å,  $b = 2.873$  Å,  $c = 14.240$  Å,  $\alpha = \beta = \gamma = 90^\circ$  ( $a = b\sqrt{3}$  – Table 3). The second set includes weaker and broader reflections (2.552, 2.404, 2.249, 2.074, 1.738 Å), systematically located on the low angle side of the strong reflections of the first set. The common indexation of the two sets of reflections leads to an orthogonal two-layer (2O) unit cell, with  $a = 5.101$  Å,  $b = 2.850$  Å,  $c = 14.240$  Å,  $\alpha = \beta = \gamma = 90^\circ$ , and  $a/b = \sqrt{3.21}$  (Table 3), these parameters being similar to those obtained for KBi<sub>10o</sub> ( $a = 5.155$  Å,  $b = 2.846$  Å,  $c = 14.088$  Å,  $\alpha = \beta =$

$\gamma = 90^\circ$ ). For this orthogonal cell, intense and weak reflections have  $11\ell$  and  $20\ell$  indices, respectively. Even though unit-cell parameters of  $\text{KBi}_{10\text{h}}$  and  $\text{KBi}_{10\text{o}}$  are similar the intensity ratio between  $20\ell$  and  $11\ell$  reflections is much lower for  $\text{KBi}_{10\text{h}}$ . The weakness of  $20\ell$  reflections could be related to the physical mixture of hexagonal  $2H$  and orthogonal  $2O$  varieties in  $\text{KBi}_{10\text{h}}$ . The presence of the  $2O$  variety is attested by the presence of 020 and 310 reflections at 1.425 Å and 1.460 Å, respectively (Table 3). In contrast, the presence of the  $2H$  variety remains uncertain because the 310,020 reflection at 1.436 Å is not clearly visible in the experimental XRD pattern of  $\text{KBi}_{10\text{h}}$ . However, the broad maximum observed at 1.431 Å could result from the overlap of the 310,020 reflection of the  $2H$  phase ( $d = 1.436$  Å) and of the 312 and 020 reflections of the  $2O$  phase ( $d = 1.430$  Å, and 1.425 Å, respectively – Figures 1, 2, Table 3).

*$\text{KBi}_{8\text{h}}$* . The three sharp peaks present at 1.448 Å, 1.426 Å and 1.398 Å (Figure 2), can be indexed with two different unit cells. The first one has an orthogonal layer symmetry and a two-layer periodicity along the  $c$  axis with  $a = 5.060$  Å,  $b = 2.855$  Å,  $c = 14.200$  Å, whereas the second one considers a hexagonal layer symmetry with  $a_{\text{ort}} = a_{\text{hex}}\sqrt{3} = 4.945$  Å,  $b_{\text{ort}} = b_{\text{hex}} = 2.855$  Å,  $c = 14.320$  Å. However,  $d(20\ell, 11\ell)$  values calculated for these two unit cells are systematically shifted with respect to the experimental ones (Table 4). Such a systematic disagreement between calculated and experimental  $d$ -values could possibly indicate a physical mixture of the  $2H$  and  $2O$  birnessite varieties. In such case, the observed discrepancy between the experimental and calculated peak positions may result from the overlap of the  $2H$  and  $2O$  reflections which usually sandwich experimental maxima. However, the positions of  $20\ell$  lines determined experimentally for the  $2O$  variety should strictly coincide with those calculated for this polytype. On the contrary, these experimental positions are systematically shifted towards the positions calculated for the  $11\ell, 20\ell$  reflections of the  $2H$  variety. As a consequence, the systematic disagreement between the experimental and calculated peak positions most likely results from the coexistence within  $\text{KBi}_{8\text{h}}$  coherent scattering domains

(CSDs) of layer fragments from both *2H* and *2O* varieties. In this case, specific diffraction effects should result from the interstratification of partially incommensurate layers, shifting  $11\ell$  and  $20\ell$  reflections, changing their relative intensity and modifying their profiles as described by Drits et al.,<sup>13,31</sup> and Lanson et al.<sup>14</sup> In addition to these structural varieties,  $\text{KBi}_{8\text{h}}$  sample contains a 3-layer rhombohedral (*3R*) birnessite-like polytype as indicated by the presence of three weak peaks at 2.412 Å, 2.144 Å, and 1.817 Å (Figure 2) which correspond respectively to 112, 115 and 118 reflections of this *3R* phase (see description of  $\text{KBi}_7$ ).

*KBi<sub>7</sub>*. As for  $\text{KBi}_{8\text{h}}$ , reflections were indexed using both *2H* and *2O* unit cells with  $a = 4.945$  Å,  $b = 2.855$  Å,  $c = 14.320$  Å,  $\alpha = \beta = \gamma = 90^\circ$  ( $a = b\sqrt{3}$ ), and  $a = 5.060$  Å,  $b = 2.855$  Å,  $c = 14.200$  Å,  $\alpha = \beta = \gamma = 90^\circ$ , respectively. As for the  $\text{KBi}_{8\text{h}}$  sample, the  $d$ -values calculated for ( $20\ell, 11\ell$ ) reflections of the *2H* phase are systematically shifted with respect to experimental ones towards those calculated for the *2O* unit cell (Table 4). Similarly, the three maxima at 2.410 Å, 2.143 Å and 1.818 Å, were indexed with a *3R* unit cell with  $a = 4.945$  Å,  $b = 2.855$  Å,  $c = 21.420$  Å,  $\alpha = \beta = \gamma = 90^\circ$  (112, 115 and 118 reflections, respectively).

*Powder XRD Patterns of Heated KBi Samples*. Additional XRD patterns were recorded *in situ* from  $\text{KBi}_{10\text{h}}$  and  $\text{KBi}_{8\text{h}}$  samples heated to 350°C under air conditions (Figure 3). For both patterns, reflections are indexed with a two-layer hexagonal (*2H*) unit cell with  $a = 4.980$  Å,  $b = 2.875$  Å,  $c = 12.995$  Å (350- $\text{KBi}_{8\text{h}}$ ), and  $a = 5.013$  Å,  $b = 2.894$  Å,  $c = 12.920$  Å (350- $\text{KBi}_{10\text{h}}$ ),  $\alpha = \beta = \gamma = 90^\circ$ , and  $a = b\sqrt{3}$  (Table 5).

**FWHM of  $20\ell$  and  $11\ell$  Reflections as a Function of  $\ell$ .** For three-dimensional (3D) periodic structures, peak broadening has two main sources.<sup>32</sup> Crystal-size broadening originates from the small CSD size and leads to an increase of the FWHM values proportional to  $1/\cos\theta$ . Strains or fluctuations of the unit cell parameters represent the second possible source of peak broadening and lead to a FWHM increase proportional to  $\tan\theta$ . After correction for either of these factors, FWHM of the reflections with identical  $hk$  values should

be similar. Accordingly, for the defect-free  $\text{KBi}_{10\text{o}}$  sample, FWHM values of  $20\ell$  and  $11\ell$  reflections are almost independent of  $\ell$  or slightly increase with  $\ell$  after correction by  $\cos\theta$  (Figure 4). For  $\text{KBi}_{10\text{h}}$  on the other hand, FWHM values dramatically decrease with  $\ell$  for  $20\ell$  reflections. Such a decrease of peak breadth with  $\ell$  should not be observed for strictly periodic structures.

**Simulation of  $\text{KBi}_{10\text{h}}$  Powder XRD Pattern.** In agreement with the model proposed by Kim et al.<sup>21</sup> and further refined by Gaillot et al.<sup>24</sup>, it is assumed that the two-layer periodicity of the  $\text{KBi}_{10\text{h}}$  structure results from the rotation of adjacent layers by  $180^\circ$  around the  $c$  axis passing through  $\text{Mn}_{\text{layer}}$ . As determined for different synthetic birnessites<sup>5,13-16,21</sup> including  $\text{KBi}_{8\text{o}}$  and  $\text{KBi}_{10\text{o}}$ <sup>24,25</sup> it is assumed that the thickness of octahedral layers is  $2.00 \text{ \AA}$ , and that Mn cations are located in the center of  $\text{MnO}_6$  octahedra. As in sample  $\text{KBi}_{10\text{o}}$ ,<sup>25</sup>  $\text{O}_{\text{layer}}$  atoms are shifted along the  $a$  axis as compared to the ideal anion close packing site ( $0.341 a$  Vs.  $0.333 a$  – Table 6) and  $\text{K}^+$  cations are located above or below the empty tridentate cavity. This site is actually split, each of the split positions being shifted in the  $ab$  plane from the center of the prismatic cavity defined by  $\text{O}_{\text{layer}}$  of adjacent layers towards one of its faces.<sup>24,25</sup> Similarly, interlayer  $\text{H}_2\text{O}$  molecules are located in the middle of the interlayer space in-between two  $\text{O}_{\text{layer}}$  from adjacent layers but slightly shifted along the  $a$  axis towards the nearest  $\text{Mn}_{\text{layer}}$  (Figure 5). Optimal coordinates of the layer and interlayer sites leading to the fits shown in Figure 6 are listed in Table 6 together with their occupancies, whereas selected interatomic distances are given in Table 7.

As compared to the experimental XRD pattern collected for  $\text{KBi}_{10\text{h}}$ , the one calculated for a defect-free  $2\text{O}$  structure with  $a_1 = 5.101 \text{ \AA}$ ,  $b_1 = 2.850 \text{ \AA}$ ,  $c = 14.240 \text{ \AA}$  exhibits  $20\ell$  maxima which are sharper and more intense than experimental ones in contrast to  $11\ell$  reflections (Figure 6a). To increase the FWHM of  $20\ell$  reflections and to decrease their

intensity,  $\text{KBi}_{10}$  is assumed to integrate several  $2O$  modifications having slightly different  $a$  and  $b$  parameters but keeping the same  $c$  parameter. To keep profiles and intensities of  $11\ell$  reflections these unit-cell parameters are related by the following relation:

$$\frac{1}{d^2(110)} = \frac{1}{a_i^2} + \frac{1}{b_i^2} \quad (4)$$

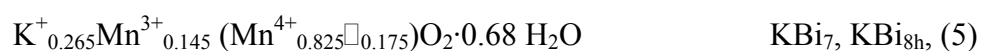
The position of  $11\ell$  reflections is unchanged for each  $2O$  modifications whose  $a$  and  $b$  parameters verify Equation (4). On the other hand,  $20\ell$  reflections of these modifications are slightly shifted to higher or lower  $2\theta$  values by decreasing or increasing their  $a$  parameter, and increasing or decreasing their  $b$  parameter, respectively. Figure 6b compares the experimental XRD pattern obtained for  $\text{KBi}_{10h}$  with those calculated for three defect-free  $2O$  modifications having slightly different layer unit-cell parameters. The XRD pattern calculated for a mixture of these three modifications exhibits  $11\ell$  reflections similar to those in each elementary XRD pattern, whereas  $20\ell$  reflections are significantly broadened, as observed in  $\text{KBi}_{10h}$  experimental pattern. In addition, intensity and positions of the  $11\ell$  reflections in  $\text{KBi}_{10h}$  experimental pattern are similar to those of  $20\ell, 11\ell$  reflections calculated for a  $2H$  modification with  $a = 4.976 \text{ \AA}$ ,  $b = 2.873 \text{ \AA}$  and  $c = 14.240 \text{ \AA}$  (Figure 6c).

Finally, the best possible fit to the experimental  $\text{KBi}_{10h}$  XRD pattern (Figure 6d –  $R_{wp} = 11.1\%$ ) was obtained for a physical mixture of three  $2O$  modifications ( $a_1 = 5.124 \text{ \AA}$ ,  $b_1 = 2.846 \text{ \AA}$ ,  $a_2 = 5.101 \text{ \AA}$ ,  $b_2 = 2.850 \text{ \AA}$ , and  $a_3 = 5.084 \text{ \AA}$ ,  $b_3 = 2.853 \text{ \AA}$  –  $c = 14.240 \text{ \AA}$ ) and of a  $2H$  phase with  $a = 4.976 \text{ \AA}$ ,  $b = 2.873 \text{ \AA}$ , and  $c = 14.240 \text{ \AA}$ . Relative proportions of these different phases are 32, 31, 13, and 24%, respectively.

**Powder XRD Pattern Simulation for  $\text{KBi}_{8h}$  and  $\text{KBi}_7$ .** From the indexation of experimental XRD patterns, the description of  $\text{KBi}_{8h}$  and  $\text{KBi}_7$  samples as a physical mixture of various  $\text{KBi}$  polytypes devoid of well-defined stacking faults may be rejected. Accordingly, all attempts to fit the experimental XRD patterns as a physical mixture of

periodic *2H*, *2O* and *3R* polytypes failed. Alternatively,  $\text{KBi}_{8\text{h}}$  and  $\text{KBi}_7$  samples can be described a mixture of elementary phases each consisting of interstratified fragments of *2H*, *2O* and *3R* polytypes. Such interstratification may shift  $11\ell$  and  $20\ell$  reflections, change their relative intensity and modify their profiles as described by Drits et al.,<sup>13,31</sup> and Lanson et al.<sup>14</sup>

*Structure of Elementary 2O, 2H, and 3R Fragments.* Atomic positions and occupancies of the various sites in the interstratified *2O* and *2H* fragments are assumed to be similar to those refined for  $\text{KBi}_{10\text{o}}$  using the Rietveld method<sup>25</sup> and for  $\text{KBi}_{8\text{o}}$  from a single crystal.<sup>24</sup> Occupancies of these sites are set according to  $\text{KBi}_{8\text{h}}$  structural formulae (Eq. 3). However, this formula should be modified to account for the migration of  $\text{Mn}^{3+}$  cations from layer to interlayer in the *2H* structure and for the resulting presence of vacant octahedra<sup>24</sup>:



However, the contrasting layer symmetry in the *2H* and *2O* varieties most likely results from different contents of  $\text{Mn}^{3+}$  cations in the  $\text{KBi}$  structure.<sup>24,25</sup> From the two structure models proposed by these authors, the  $\text{Mn}^{3+}$  content is indeed much lower in the *2H* variety than in the *2O* one. In turn, these contrasting  $\text{Mn}^{3+}$  contents give rise to different ways to minimize the steric strains arising from the elongation of  $\text{Mn}^{3+}$  octahedra, and lead in the first case to the departure of  $\text{Mn}^{3+}$  cations from layer to the interlayer (*2H* – lower  $\text{Mn}^{3+}$  content), and in the second case to an ordered distribution of  $\text{Mn}^{3+}$  cations within vacancy-free layers (*2O* – higher  $\text{Mn}^{3+}$  content). As a consequence, the proposed structural formula, which is calculated from the mean chemical parameters determined on the bulk  $\text{KBi}_{8\text{h}}$  sample, averages the relative contributions of *2H* and *2O* varieties, which are likely closer to the models proposed by Gaillot et al.<sup>24,25</sup>

In the *2H* variety, the site for interlayer  $\text{H}_2\text{O}$  is split to provide an octahedral coordination to interlayer  $\text{Mn}^{3+}$  cations on the one hand and, on the other hand, to ensure H-bonds with  $\text{O}_{\text{layer}}$  of adjacent octahedral Mn layers as in the *2O* variety. In both *2O* and *2H* polytypes, the  $\text{K}_{\text{interlayer}}$  site is split as described for  $\text{KBi}_{10\text{h}}$  (Figure 5). Atomic positions and

occupancies of the  $2H$  ( $a = 4.945 \text{ \AA}$ ,  $b = 2.855 \text{ \AA}$ ,  $c = 14.320 \text{ \AA}$ ) and  $2O$  ( $a = 5.043 \text{ \AA}$ ,  $b = 2.850 \text{ \AA}$ ,  $c = 14.240 \text{ \AA}$ ) cells providing the best fit to the experimental XRD patterns are given in Table 8. For the sake of simplicity, atomic positions and occupancies in the layers and interlayers of the  $3R$  polytype are assumed to be identical to those in the  $2H$  one.

*Diffraction Effects Resulting from the Interstratification of Elementary  $2O$ ,  $2H$ , and  $3R$  Fragments.*  $2O$  and  $2H$  fragments consists of two octahedral layers rotated with respect to each other by  $180^\circ$  around the  $c$  axis passing through  $\text{Mn}_{\text{layer}}$  site, and will be hereafter referred to as  $A$  and  $B$  fragments, respectively. These fragments differ by their  $a$  parameter ( $5.060 \text{ \AA}$  and  $4.945 \text{ \AA}$ , respectively) whereas they have the same  $b$  parameter ( $2.855 \text{ \AA}$ ). As a result, interstratified  $2O/2H$  structures consist of partly incommensurate  $A$  and  $B$  fragments. In addition, in such interstratified structures, the interlayer structure depends on the sequence of structural fragments. For example in an  $AB$  sub-sequence, the first and third interlayers are identical to those in the  $2O$  and  $2H$  polytypes, respectively, whereas the second interlayer has an intermediate structure corresponding to a "mixed"  $2O$  and  $2H$  interlayer (Figure 7).

As mentioned before, in the  $3R$  polytype octahedral layers are shifted with respect to the previous one by  $-a/3$  along the  $a$  axis. Such layer pairs are hereafter referred to as  $C$  fragments and are assumed to have layer and interlayer structures similar to those in  $B$  fragments (Table 8).  $B$  and  $C$  fragments are stacked without displacement in the  $ab$  plane in  $BB$  and  $BC$  sub-sequences whereas they are shifted with respect to each other by  $-a/3$  along the  $a$  axis in  $CB$  and  $CC$  sub-sequences (Figure 7b).

The comparison of  $\text{KBi}_{8h}$  experimental pattern with that calculated for a randomly interstratified  $2O/2H$  (60:40) mixed-layered structure (MLS – Figure 8b) shows that such interstratification induces a significant alteration of  $20\ell$  reflection profiles. With increasing  $\ell$  values the  $20\ell$  maxima appear as shoulders on the low angle side of corresponding  $11\ell$  reflections (Figure 8b). Similarly, when looking at XRD patterns calculated for  $3R/2H$  MLSs containing 75% and 15% of  $2H$  layer pairs (Figures 8d, f, respectively)  $20\ell, 11\ell$  reflections are



located between the corresponding reflections of the defect-free  $2H$  and  $3R$  polytypes in agreement with the conceptual model proposed by Drits et al.<sup>31</sup> These authors showed that for a random interstratification of layers fragments having similar thickness but different interlayer displacements observed  $hkl$  reflections are located between neighboring  $hkl$  reflections of phases whose layer fragments are interstratified, the exact position depending on the relative proportion of the elementary components.

*Description of  $KBi_{8h}$  and  $KBi_7$  Samples as a Mixture of Defective  $KBi$  Phases.* The best fit to the experimental  $KBi_{8h}$  XRD pattern (Figure 9a –  $R_{WP} = 8.2\%$ ) was obtained for a mixture of the defect-free  $2H$  polytype with interstratified  $2O/2H$ ,  $2H/3R$  and  $3R/2H$  MLSs containing respectively 40%, 75% and 15% of hexagonal layer pairs in a 9:34:48:8 ratio. The quality of the fit shown on Figure 11a pleads for a realistic description of  $KBi_{8h}$  structural heterogeneity. However, this quality relies on a significant number of adjusted parameters and the actual presence of each of the four elementary phases needs to be assessed. The respective contributions of these different MLSs to the diffracted intensity are shown on Figures 9b-d which compare the experimental  $KBi_{8h}$  pattern with those calculated for models similar to the optimal one from which one of the contributions is systematically modified or subtracted. As a result of these structural modifications, the quality of fit is systematically deteriorated in specific parts of the calculated diagram, and more specifically in the high intensity "background" regions between the main reflections, supporting the existence of each of these elementary phases.

The best fit to the experimental  $KBi_7$  pattern (Figure 10a –  $R_{WP} = 9.1\%$ ) was obtained for a mixture in a 7:29:41:23 ratio of defect-free  $2H$  polytype with interstratified  $2O/2H$  and  $2H/3R$  and  $3R/2H$  MLSs containing respectively 50%, 70%, and 10% of hexagonal layer pairs. The respective contributions of each of these elementary phases to the diffracted intensity are shown on Figures 10b-d which compare the experimental  $KBi_7$  XRD pattern with those calculated for models similar to the optimal one from which one of the

contributions is systematically modified or subtracted. As for sample  $\text{KBi}_{8h}$ , the quality of fit is then systematically deteriorated in specific parts of the experimental diagram, and more specifically in the high intensity "background" regions between the main reflections, supporting the existence of each of these elementary phases.

## Discussion

**Phase and Structural Heterogeneity of KBi.** The results obtained in the present article and in the companion papers<sup>24,25</sup> show that phase and structural heterogeneity of KBi samples synthesized at 800°C and 1000°C strongly depends on the heterogeneity of physico-chemical conditions (temperature,  $\text{PO}_2$ , ...) within the  $\text{KMnO}_4$  powder during the synthesis at these elevated temperatures. Homogeneous KBi samples are obtained when flat crucibles covered by a very thin layer of  $\text{KMnO}_4$  powder are used. For example by heating a flat crucible covered with a thin layer of  $\text{KMnO}_4$  powder ( $\sim 180 \text{ mg.cm}^{-2}$ ) to 1000°C a unique defect-free  $2O$  phase is obtained (sample  $\text{KBi}_{10o}$ ).<sup>25</sup> If the thickness of the layer of  $\text{KMnO}_4$  powder is increased as for the synthesis of  $\text{KBi}_{10h}$  ( $\sim 475 \text{ mg.cm}^{-2}$ ), the resulting product contains various  $2O$  varieties with slightly different unit-cell parameters (Table 9).

Similarly, at 800°C phase heterogeneity increases with the thickness of the layer of  $\text{KMnO}_4$  powder. In particular, the decomposition of a thin layer of  $\text{KMnO}_4$  powder ( $100 \text{ mg.cm}^{-2}$ ) covering a flat crucible leads to the formation of the defect-free  $2H$  phase in sample  $\text{KBi}_{8o}$  which contains in addition a defective interstratified  $3R/2H$  phase. Increasing the layer thickness of  $\text{KMnO}_4$  powder up to  $955 \text{ mg.cm}^{-2}$  leads to a dramatic increase of phase heterogeneity as observed for  $\text{KBi}_{8h}$  sample (Figure 9, Table 10), most likely reflecting temperature or  $\text{PO}_2$  heterogeneity within the  $\text{KMnO}_4$  powder during the synthesis.

**Structure of KBi as a Function of Synthesis Temperature.** Synthetic analogues of birnessites are usually obtained at low-to-medium temperatures, that is between 5°C<sup>1,2,11,33</sup> and 200-500°C.<sup>19,20,34,35</sup> Kim et al.<sup>21</sup> assumed that a significant increase of temperature, up to 1000°C, would promote the formation of birnessite-like compounds having a high structural perfection and a high density, which are essential parameters for the phase stability required in their sought electrochemical application. These authors were the first to obtain high-temperature KBi by using K<sup>+</sup> as interlayer cations to prevent the formation of Mn oxides with tunnel or anion close-packed structures (pillaring effect), and highly oxidizing conditions to prevent the transition towards mixed-valence oxides. As a result, a variety of synthetic birnessite in which successive layers are rotated with respect to each other by 180° around the *c* axis was obtained.<sup>21,22,24,25</sup> However, the structural characterization of KBi samples obtained at 800°C and 1000°C temperatures was confined to the determination of idealized models,<sup>21,22</sup> and additional insights in the KBi structure will be provided below.

*Layer Stacking and Symmetry.* Our experimental work and results show that temperature plays a key decisive role in the occurrence of the different layer stacking modes, as well as for layer and interlayer composition. A temperature increase from 200°C to 1000°C results in a complex sequence of structural transitions from one metastable phase to the other through intermediate mixed-layered varieties. At 400°C, the turbostratic stacking of KBi<sub>2</sub> is replaced by a highly disordered 3*R* polytype. The structural order of this 3*R* phase increases significantly by increasing temperatures to 600-700°C as attested by the presence of sharp and intense reflections (112<sub>R</sub>, 115<sub>R</sub> and 118<sub>R</sub>) which are diagnostic for this phase (Figure 1). In addition, these temperatures (600-700°C) correspond to the onset of the 2*H* polytype formation, the proportion of which increases at the expense of the 3*R* phase with increasing temperature.

The detailed phase characterization of KBi samples obtained at temperatures higher than 600°C reveals the main trends of phase transitions affecting KBi structures. With this

respect, the composition of  $\text{KBi}_7$  and  $\text{KBi}_8$  samples is especially remarkable as both samples contain the same four main phases. However the temperature increase from  $700^\circ\text{C}$  to  $800^\circ\text{C}$  leads to significant modifications between the two samples. The overall tendency is the decreasing proportion of the  $3R$  layer pairs with increasing temperature and the related increase of  $2H$  and  $2O$  layer pair proportions (Figure 11 – Table 10). This tendency is systematically observed in the four constituting phases as the proportion of  $2H$  layer pairs increases from 70 to 75% in the  $2H/3R$  MLS and from 10 to 15% in the  $3R/2H$  MLS when increasing the pyrolysis temperature from 700 to  $800^\circ\text{C}$ . In addition, the proportion of  $2O$  layer pairs in the  $2O/2H$  MLS increases from 50% in  $\text{KBi}_7$  to 60% in  $\text{KBi}_8$ , the relative proportion of this  $2O/2H$  MLS increasing slightly from  $\text{KBi}_7$  to  $\text{KBi}_{8h}$  at the expense of the  $3R/2H$  MLS (Table 10). At higher temperature ( $1000^\circ\text{C}$ )  $3R$  layer pairs are absent and the sample is overwhelmingly dominated by the  $2O$  polytype (Table 10). In  $\text{KBi}_{10h}$  phase heterogeneity is minimum as the defect-free  $2O$  phase makes up most of the sample together with a minor amount (24%) of a defect-free  $2H$  phase.

*Layer Structure.* Difference in  $\text{KBi}$  formation temperature modifies not only the layer stacking mode but also the crystal chemistry of  $\text{KBi}$  layers and interlayers. In particular, a temperature increase from  $800^\circ\text{C}$  to  $1000^\circ\text{C}$  leads to a much higher proportion of  $\text{Mn}^{3+}$  cations in the structure (0.14 in  $\text{KBi}_{8h}$  as compared to 0.24 in  $\text{KBi}_{10h}$ ). The contrasting amount of  $\text{Mn}^{3+}$  cations is combined with distinct distributions of these cations between layer and interlayer sites in the two varieties, as described earlier for the ordered  $\text{KBi}_{8o}$  and  $\text{KBi}_{10o}$  samples.<sup>24,25</sup> In  $\text{KBi}_{8o}$  interlayer  $\text{Mn}^{3+}$  cations are located above or below vacant layer octahedra in  $^{\text{VI}}\text{TC}$  sites, whereas they are present in the octahedral sites of vacancy-free layers in  $\text{KBi}_{10o}$ . In this latter variety, the unique azimuthal orientation of  $\text{Mn}^{3+}$ -octahedra, which are elongated because of Jahn-Teller distortion, leads to the departure from the hexagonal layer symmetry. However, by heating this variety up to  $350^\circ\text{C}$  it is possible to obtain a random orientation of elongated  $\text{Mn}^{3+}$  octahedra as described by Gaillot et al.<sup>25</sup>  $\text{Mn}^{3+}$ -containing

layers of edge-sharing  $\text{MnO}_6$  octahedra may have hexagonal symmetry such as in lithiophorite as a result of this random orientation with respect to the  $a$  axis ( $n60^\circ$  rotations) of  $\text{Mn}^{3+}$  octahedra. In addition to considerable lattice strains, such azimuthal distribution of  $\text{Mn}^{3+}$  octahedra leads to increased  $b$  parameters (2.925 Å in lithiophorite<sup>36</sup>) as compared to those determined for birnessites whose layers are devoid of  $\text{Mn}^{3+}$  cations or for birnessites with an ordered distribution of heterovalent Mn octahedra. For these two birnessite families the experimentally determined  $b$  parameters range 2.844 – 2.854 Å.<sup>6,13-16,24,25</sup>

Accordingly, XRD patterns recorded for samples  $\text{KBi}_{8\text{h}}$  and  $\text{KBi}_{10\text{h}}$  heated *in situ* at 350°C (350- $\text{KBi}_{8\text{h}}$  and 350- $\text{KBi}_{10\text{h}}$ , respectively) may be indexed with a unique  $2H$  phase with a  $b$  parameter equal to 2.875 Å and 2.894 Å, respectively. It should be noted that the unit-cell parameters obtained for sample  $\text{KBi}_{10\text{o}}$  heated *in situ* at 350°C ( $b = 2.895$  Å and  $c = 12.848$  Å)<sup>25</sup> almost coincide with those determined for  $\text{KBi}_{10\text{h}}$ -350 sample ( $b = 2.894$  Å and  $c = 12.920$  Å – Table 9) pleading for a similar content of  $\text{Mn}^{3+}_{\text{layer}}$  in the two samples. The different  $b$  parameters determined for 350- $\text{KBi}_{8\text{h}}$  and 350- $\text{KBi}_{10\text{h}}$  are in agreement with the contrasting contents of  $\text{Mn}^{3+}_{\text{layer}}$  in the two samples. From the comparison of Equations 2 and 5, an even stronger contrast is expected as hexagonal layers of  $\text{KBi}_{8\text{h}}$  are presumably devoid of  $\text{Mn}^{3+}$ . However  $2O$  layer pairs, which contain a significant amount of  $\text{Mn}^{3+}_{\text{layer}}$  (Table 8), represent 19% of  $\text{KBi}_{8\text{h}}$  sample and will contribute to a significant increase of the average  $b$  parameter in the  $2O/2H$  phase (Figure 10 – Table 10), leading in turn to the increase of the  $b$  parameter observed when heating sample  $\text{KBi}_{8\text{h}}$  to 350°C.

In both  $\text{KBi}_{8\text{h}}$  and  $\text{KBi}_{10\text{h}}$ , the  $2O$  polytype and  $A$  structural fragments consist of vacancy-free layers, whereas layers of the  $2H$  and  $3R$  polytypes, as well as  $B$  and  $C$  structural fragments, contain a significant proportion of vacant layer sites (up to 0.15 per octahedron – Tables 6, 8). These vacant octahedra originate mostly from the migration of  $\text{Mn}^{3+}$  cations from the layer to the interlayer. As a result,  $2O$ ,  $2H$  and  $3R$  structures have contrasting interlayer compositions and different distributions of these interlayer species. The interlayers

of the  $2O$  layer pairs are homogeneous and contain only  $K^+$  cations and associated  $H_2O$  molecules, whereas the interlayers of the  $2H$  and  $3R$  fragments are heterogeneous as they contain octahedrally coordinated  $Mn^{3+}$  cations along with  $K^+$  cations and  $H_2O$  molecules.

**KBi Heterogeneity and FWHM of Reflections in Experimental Powder XRD Patterns.** FWHM values measured for  $20\ell$  and  $11\ell$  reflections of  $KBi_{10o}$  and for  $11\ell$  maxima of sample  $KBi_{10h}$  are almost independent of  $\ell$  (Figure 4). In contrast, FWHM values measured for  $20\ell$  reflections of  $KBi_{10h}$  dramatically decrease with increasing  $\ell$  values. To account for such a contrasting behavior between  $11\ell$  and  $20\ell$  reflections of  $KBi_{10h}$ , one has to consider that  $KBi_{10h}$  consists of several  $2O$  varieties with slightly different  $a$  and  $b$  parameters but identical  $d(110)$  values. As a consequence, 11 rods corresponding to these different varieties coincide in the reciprocal lattice, whereas their 20 rods are located close to each other along the  $a^*$  axis. These latter rods are not strictly superimposed but partially overlap each other.

Diffraction effects arising from this particular case are described below. Powder X-ray diffraction effects are conventionally derived in the reciprocal space from the rotation of the reciprocal lattice with respect to a fixed Ewald sphere. Brindley and Méring proposed an alternative and effective view in which the reciprocal lattice is fixed and the radius of Ewald sphere is continuously increased.<sup>37</sup> In this alternative model, the integrated intensity at  $1/d$  sums up intensities of the reciprocal lattice nodes located on the surface of the Ewald sphere having a  $1/d$  radius. This alternative approach may be used to predict reflection profiles for a physical mixture of two phases having closely related  $a$  and  $b$  unit-cell parameters. The reciprocal lattice of a layered structure may be represented as a set of  $hk$  rods parallel to the  $c^*$  axis along which  $hk\ell$  nodes with different  $\ell$  values are located (Figure 12a).<sup>23</sup> Two partially overlapping reciprocal rods having the same  $hk$  indices and containing reflections with the same  $\ell$  values are shown on Figure 12b together with the Ewald spheres defining  $hk\ell$  reflections for these two reciprocal rods. With increasing  $\ell$  values, the two rods contribute

simultaneously to the diffracted intensity over an increased range of  $1/d$  values. This leads to a shorter distance between the respective maxima corresponding to the two overlapping reflections (dashed lines – Figure 12b) and to a lower FWHM for the resulting combined diffraction maximum (Figure 12b) as observed experimentally after correction for crystal-size broadening. The observed decrease of the  $20\ell$  reflection FWHM with increasing  $\ell$  values (Figure 4) can thus be considered as an independent evidence of such type of phase heterogeneity. Because all  $2O$  varieties have identical  $d(110)$  values,  $11$  reciprocal rods completely overlap in the reciprocal space and, as a consequence, the FWHM of  $11\ell$  reflections is independent of  $\ell$  despite the differences in  $a$  and  $b$  parameters. One may note (Figure 4) that for the homogeneous  $\text{KBi}_{100}$  sample the correlations between FWHM and  $\ell$  for  $20\ell$  and  $11\ell$  reflections lead to slightly different slopes. This difference most likely reflects the presence in this sample of a small proportion of particles having  $2O$  structure and unit-cell parameters slightly different from those of the main  $2O$  phase. The relation between the FWHM of  $11\ell, 20\ell$  reflection and the  $\ell$  indice may be used as an independent criterion to estimate the degree of phase heterogeneity in KBi samples.

**Origin of the Structural Heterogeneity for  $\text{KBi}_{10h}$ .** Heterogeneous heating to  $\sim 1000^\circ\text{C}$  of individual  $\text{KMnO}_4$  particles leads essentially to the formation of KBi crystals having different  $a$  and  $b$  parameters. The  $a/b$  ratios obtained for the three identified sub-populations of KBi crystals range 1.784-1.800 (Table 9) as a consequence of lattice distortion induced by the Jahn-Teller distortion of  $\text{Mn}^{3+}$  octahedra. Two hypotheses may account for the observed scatter of the  $a/b$  ratio. The first one is the local fluctuation of the redox conditions in which individual KBi crystals are formed resulting in the presence of contrasting amounts of  $\text{Mn}^{3+}$  cations from one crystal to the other. According to the other hypothesis, all KBi crystals have almost the same content of  $\text{Mn}^{3+}$  cations but differ from each other by their respective mean orientation of the long  $\text{Mn}^{3+}\text{-O}$  bonds with respect to the  $a$  axis. In this

second hypothesis, the maximum  $a/b$  ratio likely correspond to crystals in which most or all  $\text{Mn}^{3+}$  octahedra are elongated along the  $a$  axis, whereas in crystals with the minimum  $a/b$  ratio the long  $\text{Mn}^{3+}$ -O bonds of some  $\text{Mn}^{3+}$  octahedra are likely oriented at  $\pm 60^\circ$  with respect to the  $a$  axis. Such different azimuthal orientations of elongated  $\text{Mn}^{3+}$  octahedra should result in an increased  $b$  parameter whereas the  $a$  parameter should decrease, as observed experimentally. After heating to  $350^\circ\text{C}$  the FWHM of  $11\ell, 20\ell$  reflections recorded for 350-KBi<sub>10o</sub> and 350-KBi<sub>10h</sub> are almost independent of  $\ell$  (Figure 13) pleading for a similar content of  $\text{Mn}^{4+}$  and  $\text{Mn}^{3+}$  in all KBi<sub>10h</sub> crystals, as in KBi<sub>10o</sub>. The similar unit-cell parameters obtained for 350-KBi<sub>10o</sub> and 350-KBi<sub>10h</sub> (2.894 Å vs. 2.895 Å, respectively) also support this second hypothesis of a partial disorientation of  $\text{Mn}^{3+}$  octahedra with respect to the  $a$  axis. It should be noted that the presence of the  $2H$  polytype, even though minor, does not affect the FWHM of  $11\ell, 20\ell$  reflections recorded for 350-KBi<sub>10h</sub>. This is likely due to the presence of a relatively high amount of  $\text{Mn}^{3+}_{\text{layer}}$  in the layers building up this  $2H$  polytype (Table 6). This hypothesis is supported by the high value (2.873 Å – Table 9) determined for the  $b$  parameter of this  $2H$  polytype. As discussed above, such a high  $b$  parameter most likely results from the random orientation of elongated  $\text{Mn}^{3+}$  octahedra within the octahedral layer of birnessite.

**Origin of the Structural Heterogeneity for KBi<sub>8h</sub>.** KBi<sub>8h</sub> is a complex physical mixture of a periodic  $2H$  phase and of various  $2O/2H$  and  $3R/2H$  MLSs. In these different phases, individual layers have different layer symmetry most likely resulting from contrasting contents of  $\text{Mn}^{3+}_{\text{layer}}$ . As described above, *A* fragments likely consist of vacancy-free layers containing a significant amount of  $\text{Mn}^{3+}_{\text{layer}}$  (~25%) whereas *B* and *C* fragments are likely devoid of  $\text{Mn}^{3+}_{\text{layer}}$  cations as a result of their layer-to-interlayer migration. As can be seen in Figure 13, the FWHM values measured for 350-KBi<sub>8h</sub> sample decrease systematically with increasing  $\ell$  values to indicate the coexistence of crystals with close but different unit-cell parameters as described above. The difference of unit-cell parameters after heating to  $350^\circ\text{C}$



and the induced random orientation of elongated  $\text{Mn}^{3+}$  octahedra likely originates from the coexistence of crystals with contrasting contents of  $\text{Mn}^{3+}_{\text{layer}}$ . By combining chemical data (Equations 3 and 5) and structural details derived from XRD simulations (Table 8), it is possible to propose the following structural formulae for  $2O$  fragments on the one hand and for  $2H$  and  $3R$  ones on the other hand:



The resulting mean oxidation degree Mn ( $3.79 \times 19\% + 3.88 \times 81\% = 3.86$ ) is compatible with that determined experimentally (3.85 – Table 1) by combining chemical data (Equations 3 and 5) and structural details derived from XRD.

**New Type of Structural Disorder in Birnessite.** Except for the frequent presence of random stacking faults, two types structural defects are extremely common in layered structures. The random interstratification of layers having different thicknesses, which is the first type of such structural disorder, is especially widespread in mixed-layered clay minerals.<sup>38</sup> Well defined stacking faults, which make the other type of structural disorder, are conveniently described as resulting from the interstratification of layers having similar thickness but different interlayer displacements.<sup>31</sup>

The random interstratification of  $2O$  (A) and  $2H$  (B) structural fragments in the  $2O/2H$  phase described in both  $\text{KBi}_7$  and  $\text{KBi}_{8h}$  represents a new type of structural disorder in lamellar structures. In this specific case, interstratified layers have the same thickness and the same interlayer stacking mode, but their layer dimensions in the  $ab$  plane are incommensurate. Such crystal structures consisting of alternating layers having different unit-cell parameters have been previously reported in the literature. For example, alternation of incommensurate layers has been described in the structures of asbolanes,<sup>39</sup> valleriite and tochilinite.<sup>40-42</sup> However, in all these "hybrid structures"<sup>40</sup> incommensurate layers are

regularly alternating along the  $c$  axis and their structures may be described by a set of unit cells, which have not only different sizes but also different shapes.

In contrast, the  $2O$  and  $2H$  structural fragments having different  $a$  parameters are randomly interstratified in the  $2O/2H$  phase, and the description of the diffraction effects by such a structure should be analogous to that developed for mixed-layered structures<sup>23,43,44</sup> and for the structures containing stacking faults.<sup>23,29,45</sup> In the reciprocal space, 11 rods of the interstratified fragments completely overlap each other because of their identical  $d(110)$  values leading to the coherence of the diffracted waves for  $11\ell$  reflections. A similar effect exists for the  $20\ell$  and  $11\ell$  reflections of the hexagonal fragments as these reflections coincide with  $11\ell$  reflections of the  $2O$  fragments. Such a high coherence gives rise to the sharp and intense maxima observed for the combined  $20\ell, 11\ell$  reflections of the  $2H$  fragments and  $11\ell$  reflections of the  $2O$  fragments (Figures 2, 9, 10). In contrast, a significant phase misfit arises for the incomplete overlap of 20 rods from  $2O$  fragments with those of the  $2H$  fragments leading to a significant loss of coherence of the diffracted waves when  $2O$  and  $2H$  fragments are interstratified. As a result,  $20\ell$  reflections of the  $2O$  fragments are broadened and shifted towards the partially overlapped  $20\ell, 11\ell$  and  $11\ell$  reflections scattered by the  $2H$  and  $2O$  layer pairs, respectively, and are only observed as diffuse shoulders (Figures 9, 10).

## Acknowledgements

VAD is grateful to the Environmental Geochemistry Group of the LGIT (Grenoble, France) and to the Russian Science Foundation for financial support. BL acknowledges financial support from INSU/Géomatériaux, and CNRS/PICS709 programs. Céline Boissard (Hydr'ASA – Poitiers), Martine Musso and Delphine Tisserand (LGIT – Grenoble) are thanked for their technical support (DT-TG analyses and chemical analyses, respectively).

## Literature cited

- (1) Giovanoli, R.; Stähli, E.; Feitknecht, W. *Helv. Chim. Acta* **1970**, *53*, 209-220.
- (2) Giovanoli, R.; Stähli, E.; Feitknecht, W. *Helv. Chim. Acta* **1970**, *53*, 453-464.
- (3) Burns, R. G.; Burns, V. M. *Phil Trans Roy Soc London A* **1977**, *286*, 283-301.
- (4) Chukhrov, F. V.; Gorschkov, A. I.; Rudnitskaya, E. S.; Sivtsov, A. V. *Izv. Akad. Nauk Geol.* **1978**, *9*, 67-76.
- (5) Post, J. E.; Veblen, D. R. *Amer. Mineral.* **1990**, *75*, 477-489.
- (6) Drits, V. A.; Silvester, E. J.; Gorshkov, A. I.; Manceau, A. *Amer. Mineral.* **1997**, *82*, 946-961.
- (7) Drits, V. A.; Lanson, B.; Bougerol Chaillout, C.; Gorshkov, A. I.; Manceau, A. *Amer. Mineral.* **2002**, *87*, 1646-1661.
- (8) Manceau, A.; Schlegel, M. L.; Chateigner, D.; Lanson, B.; Bartoli, C.; Gates, W. P. In *Synchrotron X-ray methods in clay science*; Schulze, D. G., Stucki, J. W., Bertsch, P. M., Eds.; Clay Minerals Society: Boulder, Co, 1999; Vol. 9, pp 68-114.
- (9) Manceau, A.; Lanson, B.; Drits, V. A. *Geochim. Cosmochim. Acta* **2002**, *66*, 2639-2663.
- (10) Kuma, K.; Usui, A.; Paplawsky, W.; Gedulin, B.; Arrhenius, G. *Miner. Mag.* **1994**, *58*, 425-447.
- (11) Silvester, E. J.; Manceau, A.; Drits, V. A. *Amer. Mineral.* **1997**, *82*, 962-978.
- (12) Manceau, A.; Drits, V. A.; Silvester, E. J.; Bartoli, C.; Lanson, B. *Amer. Mineral.* **1997**, *82*, 1150-1175.
- (13) Drits, V. A.; Lanson, B.; Gorshkov, A. I.; Manceau, A. *Amer. Mineral.* **1998**, *83*, 97-118.
- (14) Lanson, B.; Drits, V. A.; Silvester, E. J.; Manceau, A. *Amer. Mineral.* **2000**, *85*, 826-838.

- 665 (15) Lanson, B.; Drits, V. A.; Feng, Q.; Manceau, A. *Amer. Mineral.* **2002**, 87,  
666 1662-1671.
- 667 (16) Lanson, B.; Drits, V. A.; Gaillot, A. C.; Silvester, E.; Plancon, A.; Manceau, A.  
668 *Amer. Mineral.* **2002**, 87, 1631-1645.
- 669 (17) Le Goff, P.; Baffier, N.; Bach, S.; Pereira-Ramos, J. P.; Messina, R. *Solid State*  
670 *Ionics* **1993**, 61, 309-315.
- 671 (18) Le Goff, P.; Baffier, N.; Bach, S.; Pereira-Ramos, J.-P. *J. Mater. Chem.* **1994**,  
672 4, 875-881.
- 673 (19) Chen, R. J.; Zavalij, P.; Whittingham, M. S. *Chem. Mater.* **1996**, 8, 1275-1280.
- 674 (20) Chen, R. J.; Chirayil, T.; Zavalij, P.; Whittingham, M. S. *Solid State Ionics*  
675 **1996**, 86-88, 1-7.
- 676 (21) Kim, S. H.; Kim, S. J.; Oh, S. M. *Chem. Mater.* **1999**, 11, 557-563.
- 677 (22) Kim, S. H.; Im, W. M.; Hong, J. K.; Oh, S. M. *J. Electrochem. Soc.* **2000**, 147,  
678 413-419.
- 679 (23) Drits, V. A.; Tchoubar, C. *X-ray diffraction by disordered lamellar structures:*  
680 *Theory and applications to microdivided silicates and carbons*; Springer-Verlag: Berlin,  
681 1990.
- 682 (24) Gaillot, A.-C.; Drits, V. A.; Flot, D.; Manceau, A.; Burghammer, M.; Lanson,  
683 B. *Chem. Mater.* **2003**, 15, 4666-4678.
- 684 (25) Gaillot, A.-C.; Drits, V. A.; Lanson, B.; Manceau, A. *Chem. Mater.* **2004**, *In*  
685 *preparation*.
- 686 (26) Vetter, K. J.; Jaeger, N. *Electrochim. Acta* **1966**, 11, 401-419.
- 687 (27) Lingane, J. J.; Karplus, R. *Ind. Eng. Chem. Anal. Ed.* **1946**, 18, 191-194.
- 688 (28) Chukhrov, F. V.; Sakharov, B. A.; Gorshkov, A. I.; Drits, V. A.; Dikov, Y. P.  
689 *Int. Geol. Rev.* **1985**, 27, 1082-1088.
- 690 (29) Plançon, A., Ph. D. Thesis, Orléans, France, 1976.

- 691 (30) Brindley, G. W. In *Crystal Structures of Clay Minerals and their X-ray*  
692 *Identification*; Brindley, G. W., Brown, G., Eds.; Mineralogical Society: London, 1980, pp  
693 125-195.
- 694 (31) Drits, V. A.; McCarty, D. K. *Amer. Mineral.* **1996**, *81*, 852-863.
- 695 (32) Klug, H. P.; Alexander, L. E. *X-ray diffraction procedures for polycrystalline*  
696 *and amorphous materials*; Wiley: New York, 1974.
- 697 (33) Bach, S.; Pereira-Ramos, J. P.; Baffier, N. *J. Solid State Chem.* **1995**, *120*, 70-  
698 73.
- 699 (34) Ching, S.; Roark, J. L.; Duan, N.; Suib, S. L. *Chem. Mater.* **1997**, *9*, 750-754.
- 700 (35) Ching, S.; Landrigan, J. A.; Jorgensen, M. L.; Duan, N.; Suib, S. L.; O'Young,  
701 C. L. *Chem. Mater.* **1995**, *7*, 1604-1606.
- 702 (36) Post, J. E.; Appleman, D. E. *Amer. Mineral.* **1988**, *73*, 1401-1404.
- 703 (37) Brindley, G. W.; Méring, J. *Acta Crystallogr.* **1951**, *4*, 441-447.
- 704 (38) Moore, D. M.; Reynolds, R. C., Jr *X-ray Diffraction and the Identification and*  
705 *Analysis of Clay Minerals*; Oxford University Press, 1989.
- 706 (39) Chukhrov, F. V.; Gorshkov, A. I.; Drits, V. A. *Izv. Akad. Nauk Geol.* **1982**, *6*,  
707 69-77 (in Russian).
- 708 (40) Evans, H. T.; Allman, R. Z. *Kristallogr.* **1968**, *127*, 73-93.
- 709 (41) Drits, V. A. *Electron diffraction and high-resolution electron microscopy of*  
710 *mineral structures*; Springer Verlag: Berlin Heidelberg, 1987.
- 711 (42) Organova, N. I.; Drits, V. A.; Dimitrik, A. L. *Amer. Mineral.* **1974**, *59*, 190-  
712 200.
- 713 (43) Drits, V. A.; Sakharov, B. A. *X-Ray structure analysis of mixed-layer minerals*;  
714 Nauka: Moscow, 1976.

(44) Reynolds, R. C., Jr In *Crystal structures of clay minerals and their X-ray identification*; Brindley, G. W., Brown, G., Eds.; The Mineralogical Society: London, 1980, pp 249-359.

(45) Plançon, A. *J. Appl. Cryst.* **1981**, *14*, 300-304.

### Figure captions

**Figure 1.** Experimental XRD patterns of KBi samples obtained from thermal decomposition of  $\text{KMnO}_4$  at temperatures varying from  $1000^\circ\text{C}$  to  $200^\circ\text{C}$  (from top to bottom). Dashed lines outline the position of  $00\ell$  reflections, whereas dot-dashed lines indicate the positions of reflections of KBi  $3R$  polytype. Intensity scale is enlarged over the  $30\text{-}80^\circ 2\theta$   $\text{CuK}\alpha$  range.

**Figure 2.** Experimental XRD patterns of KBi samples obtained from thermal decomposition of  $\text{KMnO}_4$  at temperatures varying from  $1000^\circ\text{C}$  to  $700^\circ\text{C}$  (from top to bottom). Dashed lines outline the position of  $31\ell$  and  $02\ell$  reflections, whereas dot-dashed lines indicate the positions of reflections of KBi  $3R$  polytype. Diffraction maxima are indexed in terms of the  $2O$ ,  $2H$  and  $3R$  polytypes identified in these samples (Tables 3 and 4).

**Figure 3.** Experimental XRD patterns of  $\text{KBi}_{10\text{h}}$  (top) and  $\text{KBi}_{8\text{h}}$  (bottom) samples recorded *in situ* at  $350^\circ\text{C}$ . Diffraction maxima are indexed in terms of the  $2H$  polytype identified in these samples (Table 5). Stars indicate the  $11\ell$  reflections of a  $3R$ -type phase as listed in Table 5.

**Figure 4.** Evolution of the full width at half maximum intensity (FWHM) for  $20\ell$  and  $11\ell$  reflections (circles and triangles, respectively) as a function of the Miller index  $\ell$ . FWHM are corrected by  $\cos\theta$ . Homogeneous  $\text{KBi}_{10\text{o}}^{25}$  and heterogeneous  $\text{KBi}_{10\text{h}}$  samples are shown respectively at the top and the bottom.

**Figure 5.** Structure model for  $\text{KBi}_{10\text{h}}$ . **a)** Projection on the  $ab$  plane. The upper surface of the lower layer is shown as light shaded triangles.  $\text{O}_{\text{layer}}$  and  $\text{Mn}_{\text{layer}}$  of this lower layer are shown as small solid and large open circles, respectively. Large shaded circles = interlayer

potassium. Interlayer H<sub>2</sub>O molecules are shown as large open circles with a dashed outline. **b)** Projection along the *b* axis. Open and solid symbols indicate atoms at *y* = 0, and at *y* = ±1/2, respectively. Small circles represent O<sub>layer</sub> atoms, large circles represent Mn<sub>layer</sub> atoms, squares represent vacant layer octahedra. Dot-dashed lines outline the interlayer prisms defined by the two empty tridentate layer cavities. The center of these prisms is shown by regular dashed lines, and the arrow outlines the shift of K cations from this ideal position.

**Figure 6.** Comparison between experimental and calculated XRD patterns for KBi<sub>10h</sub>. Experimental data are shown as crosses, whereas calculated profiles are shown as solid lines. Only 20 $\ell$  and 11 $\ell$  reflections are calculated. Atomic coordinates and other structural parameters used for the calculations are listed in Tables 6, 9, and 10. **(a)** Calculation for a unique 2*O* polytype (2*O*<sub>2</sub>). **(b)** Calculation made assuming the presence of three 2*O* polytypes having slightly different unit-cell parameters. 2*O*<sub>1</sub>, 2*O*<sub>2</sub>, and 2*O*<sub>3</sub>, are shown as dashed, solid, and dot-dashed lines, respectively. **(c)** Calculation made for a 2*H* polytype. **(d)** Optimum model and difference plot.

**Figure 7.** Schematic view along the *b* axis of the interlayer structure in mixed-layered structures (MLSs) of different KBi polytypes. Interlayers of the 2*O* polytype (A fragments) are shown as small solid circles, whereas those of 2*H* and 3*R* polytypes (B and C fragments, respectively) are shown as small solid triangles. Respective orientations of successive layers in the different polytypes are schematized by the orientations of Mn octahedra in projection along the *b* axis. The increased *a* parameter of the A fragments, as compared to B and C fragments, is symbolized by the elongation of projected Mn octahedra. 2*O*/2*H* and 2*H*/3*R* MLSs are described in the top and bottom parts of the figure, respectively.

**Figure 8.** Comparison between experimental and calculated XRD patterns for KBi<sub>8h</sub>. Patterns as in Figure 6. Only 20 $\ell$  and 11 $\ell$  reflections are calculated. Atomic coordinates and other structural parameters used for the calculations are listed in Tables 8 and 9. **(a)** Calculation made for a defect-free 2*O* phase. **(b)** Calculation made for a 2*O*/2*H* MLSs (2*O*:2*H* ratio

60:40). (c) Calculation made for a defect-free  $2H$  phase. (d) Calculation made for a  $2H/3R$  MLSs ( $2H:3R$  ratio 75:25). (e) Calculation made for a  $3R/2H$  MLSs ( $3R:2H$  ratio 85:15). (f) Calculation made for a defect-free  $3R$  phase.

**Figure 9.** Comparison between experimental and calculated XRD patterns for  $\text{KBi}_{8h}$ . Patterns as in Figure 6. Only  $20\ell$  and  $11\ell$  reflections are calculated. Atomic coordinates and other structural parameters used for the calculations are listed in Tables 8, 9, and 10. Arrows outline the misfits between experimental and calculated patterns. (a) Optimum model and difference plot. The optimum model includes contributions from a defect-free  $2H$  polytype and from  $2O/2H$ ,  $2H/3R$ , and  $3R/2H$  MLSs (Relative proportions 9:34:48:8 – Table 10). (b) Calculation made replacing the optimum  $2O/2H$  contribution ( $2O:2H$  ratio 60:40) by a defect-free  $2H$  contribution. (c) Calculation made by subtracting the  $2H/3R$  contribution ( $2H:3R$  ratio 75:25) from the optimum model. (d) Calculation made by subtracting the  $3R/2H$  contribution ( $3R:2H$  ratio 85:15) from the optimum model.

**Figure 10.** Comparison between experimental and calculated XRD patterns for  $\text{KBi}_7$ . Patterns as in Figure 6. Only  $20\ell$  and  $11\ell$  reflections are calculated. Atomic coordinates and other structural parameters used for the calculations are listed in Tables 8, 9, and 10. Arrows outline the misfits between experimental and calculated patterns. (a) Optimum model and difference plot. The optimum model includes contributions from a defect-free  $2H$  polytype and from  $2O/2H$ ,  $2H/3R$ , and  $3R/2H$  MLSs (Relative proportions 7:29:41:23 – Table 10). (b) Calculation made replacing the optimum  $2O/2H$  contribution ( $2O:2H$  ratio 50:50) by a defect-free  $2H$  contribution. (c) Calculation made by subtracting the  $2H/3R$  contribution ( $2H:3R$  ratio 70:30) from the optimum model. (d) Calculation made by subtracting the  $3R/2H$  contribution ( $3R:2H$  ratio 90:10) from the optimum model.

**Figure 11.** Relative proportions of  $3R$ ,  $2H$ , and  $2O$  layer pairs (solid bars, shaded bars, and open bars, respectively) in  $\text{KBi}$  samples as a function of the pyrolysis temperature.



**Figure 12.** (a) Schematic description of the intensity diffracted at a  $hk\ell$  node (shaded ellipsoid) by the intersection of a  $hk$  rod (dot-dashed cylinder) with Ewald spheres (radii ranging  $1/d'-1/d''$ ). The distribution of intensity within the  $hk\ell$  node is schematized by the intensity of the gray shading. (b) Schematic description of the intensity diffracted at two partially overlapping  $hk\ell$  nodes (shaded cylinders) by the intersection of  $hk$  rods (with dot-dashed and solid outlines, respectively) with Ewald spheres of increasing radii. The positions of  $hk\ell$  reflections barycenters are outlined by dashed lines. On the right side of the figure the breadth of resulting  $hk\ell$  reflection is shown as a function of the  $z^*$  coordinate along the  $c^*$  axis. Reflection broadening with increasing  $z^*$  coordinate resulting from the intensity distribution within the  $hk\ell$  node is not represented.

**Figure 13.** Evolution of the FWHM for  $20\ell$ ,  $11\ell$  reflections as a function of the Miller index  $\ell$ . FWHM of the  $K\alpha_2$ -stripped lines are corrected by  $\cos\theta$ . Heterogeneous 350-KBi<sub>8h</sub>, heterogeneous 350-KBi<sub>10h</sub>, and homogeneous 350-KBi<sub>10o</sub><sup>25</sup> samples are shown as solid diamonds, solid triangles, and solid squares, respectively.

**Table 1.** Experimental conditions (shape and size of crucible and density of  $\text{KMnO}_4$  powder) used for the synthesis of the KBi samples.

Sample	Amount of $\text{KMnO}_4$ powder	Surface area (crucible)	Density of powder ( $\text{mg}/\text{cm}^2$ )
$\text{KBi}_{10\text{o}}$ (homogeneous) <sup>a</sup>	2g	$4.5 \times 2.5 \text{ cm}^2$	178
$\text{KBi}_{10\text{h}}$	1.5g	$\pi \times 1^2 \text{ cm}^2$	477
$\text{KBi}_{8\text{o}}$ (homogeneous) <sup>b</sup>	3g	$6.8 \times 4.45 \text{ cm}^2$	100
$\text{KBi}_{8\text{h}}$	3g	$\pi \times 1^2 \text{ cm}^2$	955
$\text{KBi}_7$	1g	$4.5 \times 2.5 \text{ cm}^2$	89
$\text{KBi}_6$	2g	$\pi \times 2.25^2 \text{ cm}^2$	126
$\text{KBi}_4$	2g	$\pi \times 2.25^2 \text{ cm}^2$	126
$\text{KBi}_2$	2g	$\pi \times 2.25^2 \text{ cm}^2$	126

*Note:* <sup>a</sup> Sample described by Gaillot et al.<sup>25</sup> <sup>b</sup> Sample described by Gaillot et al.<sup>24</sup>

**Table 2.** Main chemical parameters of KBi samples

	$\text{KBi}_7$	$\text{KBi}_{8\text{h}}$	$\text{KBi}_{10\text{h}}$
Weight loss due to interlayer $\text{H}_2\text{O}$	6.3%	6.5%	8.9%
Weight loss due to hydroxyl groups	2.6%	2.3 %	-
$\text{H}_2\text{O}/\text{Mn}$ ratio	0.70	0.68	0.53
K/Mn ratio	0.270	0.274	0.271
Mn mean oxidation state	3.87	3.85	3.78

*Note:* K/Mn ratio is determined by ICP-AES. Weight losses correspond to the first two endotherms ( $\sim 150^\circ\text{C}$  and  $370^\circ\text{C}$ , respectively) observed on the DTA-TG curves.  $\text{H}_2\text{O}/\text{Mn}$  ratio includes both interlayer  $\text{H}_2\text{O}$  and hydroxyl groups.

**Table 3.** Indexing of the experimental XRD pattern of  $\text{KBi}_{10\text{h}}$  with  $2O$  and  $2H$  cells.

<b><math>2H</math> polytype</b>			<b><math>2O</math> polytype</b>	
$d_{\text{exp}} (hkl)$	$hkl$	$d_{\text{cal}} (hkl)$	$hkl$	$d_{\text{cal}} (hkl)$
7.705 <sup>a</sup>				
7.131	002	7.120	002	7.120
4.404 <sup>a</sup>				
3.700 <sup>a</sup>				
3.562	004	3.560	004	3.560
2.750 <sup>a</sup>				
2.552			200	2.551
2.485	200, 110	2.488	110	2.488
2.451	201, 111	2.451	111	2.451
2.404			202	2.401
2.347	202, 112	2.349	112	2.349
2.249			203	2.247
2.204	203, 113	2.204	113	2.204
2.074			204	2.073
2.040	204, 114	2.039	114	2.039
1.898			205	1.900
1.874	205, 115	1.874	115	1.874
1.781	008	1.780	008	1.780
1.738			206	1.737
1.718	206, 116	1.717	116	1.717
1.460			208 / 310	1.460
1.448	208, 118	1.448	118	1.448
1.431	310, 020	1.436	312	1.430
1.425			020	1.425
1.397	312, 022	1.408	022	1.397
1.352			314	1.351
1.344			209	1.345
1.334	209, 119	1.335	119	1.335
	314, 024	1.332		
1.323			024	1.323
1.243	220, 400	1.244	220 / 316	1.244
			20.10	1.243
1.236	221, 401	1.239	221 / 11.10	1.239 / 1.236
1.225	316, 026	1.229		
	222, 402	1.225	222 / 026	1.225 / 1.222
1.204	223, 403	1.203	223	1.203
1.174	224, 404	1.174	224	1.174
1.128			318 / 406	1.129 / 1.123
1.102	226, 406	1.102	226	1.102

*Note:*  $a = 4.976 \text{ \AA}$ ,  $b = 2.873 \text{ \AA}$ ,  $c = 14.240 \text{ \AA}$ ,  $\alpha = \beta = \gamma = 90^\circ$  ( $2H$  polytype), and  $a = 5.101 \text{ \AA}$ ,  $b = 2.850 \text{ \AA}$ ,  $c = 14.240 \text{ \AA}$ ,  $\alpha = \beta = \gamma = 90^\circ$  ( $2O$  polytype). Calculated  $d_{\text{cal}} (hkl)$  reflection positions (in  $\text{\AA}$ ) are compared to experimental  $d_{\text{exp}} (hkl)$  ones. <sup>a</sup> indicates additional lines related to the supercell of the  $2O$  polytype.<sup>25</sup>

**Table 4.** Indexing of the experimental XRD patterns of  $\text{KBi}_{8h}$  and  $\text{KBi}_7$  with  $2O$ ,  $2H$ , and  $3R$  cells.

<b><math>\text{KBi}_7</math></b>	<b><math>\text{KBi}_{8h}</math></b>	<b><math>2H</math> polytype</b>		<b><math>2O</math> polytype</b>		<b><math>3R</math> polytype</b>	
$d_{\text{exp}} (hkl)$	$d_{\text{exp}} (hkl)$	$hkl$	$d_{\text{cal}} (hkl)$	$hkl$	$d_{\text{cal}} (hkl)$	$hkl$	$d_{\text{cal}} (hkl)$
7.140	7.136	002	7.160	002	7.110	003	7.140
3.574	3.567	004	3.580	004	3.555	006	3.570
2.514	2.517			200	2.530		
2.479				110	2.487		
2.471	2.472	200, 110	2.473				
2.456				111	2.449	201	2.456
	2.428	201, 111	2.436				
2.410	2.412					112	2.409
2.378	2.378	006	2.387	202, 006	2.384, 2.370	009	2.380
2.341	2.342	202, 112	2.337	112	2.347		
2.223	2.218			203	2.232	204	2.245
2.195	2.196	203, 113	2.195	113	2.202		
2.143	2.144					115	2.141
	2.058			204	2.061		
2.036	2.036	204, 114	2.034	114	2.038		
1.929						207	1.923
1.871	1.871	205, 115	1.872	115	1.872		
1.818	1.817					118	1.816
1.785	1.785	008	1.790	008	1.778	00.12	1.785
	1.728			206	1.730		
1.717	1.717	206, 116	1.717	116	1.716		
1.626						20.10	1.619
1.531						11.11	1.530
1.448	1.448	208, 118	1.450	208, 310, 118	1.454, 1.452, 1.446		
1.426	1.426	310, 020	1.427	020, 312	1.428, 1.423	310, 020	1.427
1.416				00.10	1.422		
1.399	1.398	312, 022	1.400	022	1.400	313, 023	1.400
1.340	1.338	209, 119	1.338	314, 119	1.344, 1.332		
1.325	1.325	314, 024	1.326	024	1.325	316, 026	1.325
1.235	1.237	20.10, 11.10	1.238	316	1.238		
		400, 220	1.236	11.10	1.234	221	1.234
		316, 026	1.225	222	1.225	402	1.228
1.223	1.222	402, 222	1.218	026	1.223	319, 029	1.224
1.191	1.190	403, 223	1.197	404	1.192	224	1.205
1.169	1.170	404, 224	1.169	224	1.174	405	1.188
	1.114	318, 028	1.116	406, 028	1.116, 1.113	31.12, 02.12	1.115

*Note:*  $a = 4.945 \text{ \AA}$ ,  $b = 2.855 \text{ \AA}$ ,  $c = 14.320 \text{ \AA}$  ( $2H$  polytype),  $a = 5.060 \text{ \AA}$ ,  $b = 2.855 \text{ \AA}$ ,  $c = 14.200 \text{ \AA}$  ( $2O$  polytype), and  $a = 4.945 \text{ \AA}$ ,  $b = 2.855 \text{ \AA}$ ,  $c = 21.420 \text{ \AA}$  ( $3R$  polytype).  $\alpha = \beta = \gamma = 90^\circ$  for all three polytypes. Calculated  $d_{\text{cal}} (hkl)$  reflection positions (in  $\text{\AA}$ ) are compared to experimental  $d_{\text{exp}} (hkl)$  ones.

**Table 5.** Indexing of the experimental XRD patterns of  $\text{KBi}_{10\text{h}}$  and  $\text{KBi}_{8\text{h}}$  recorded *in situ* at  $350^\circ\text{C}$  with a  $2H$  cell.

350- $\text{KBi}_{10\text{h}}$			350- $\text{KBi}_{8\text{h}}$	
$hkl$	$d_{\text{exp}} (hkl)$	$d_{\text{cal}} (hkl)$	$d_{\text{exp}} (hkl)$	$d_{\text{cal}} (hkl)$
002	6.471 4.818 <sup>a</sup> 4.332 <sup>a</sup> 4.124 <sup>a</sup>	6.460	6.506	6.498
004	3.231	3.230	3.248	3.249
200, 110	2.504	2.506	2.490	2.490
201, 111	2.462	2.460	2.423 <sup>b</sup>	
202, 112	2.336	2.337	2.326	2.325
203, 113	2.166	2.166	2.159 2.096 <sup>b</sup>	2.159
204, 114	1.980	1.980	1.976	1.976
205, 115	1.801	1.799	1.785 <sup>b</sup>	1.798
206, 116	1.634	1.633	1.634	1.634
008	1.618	1.615	1.618	1.624
310, 020	1.447	1.447	1.437	1.438
312, 022	1.412	1.412	1.403	1.404
208, 118			1.360	1.360
314, 024			1.313	1.315
400, 220			1.242	1.245
402, 222			1.221	1.223
316, 026			1.193	1.198
404, 224			1.152	1.162

*Note:*  $a = 5.013 \text{ \AA}$ ,  $b = 2.894 \text{ \AA}$ ,  $c = 12.920 \text{ \AA}$  (350- $\text{KBi}_{10\text{h}}$  sample), and  $a = 4.980 \text{ \AA}$ ,  $b = 2.875 \text{ \AA}$ ,  $c = 12.995 \text{ \AA}$  (350- $\text{KBi}_{8\text{h}}$  sample).  $\alpha = \beta = \gamma = 90^\circ$  for the two samples. Calculated  $d_{\text{cal}} (hkl)$  reflection positions (in  $\text{\AA}$ ) are compared to experimental  $d_{\text{exp}} (hkl)$  ones. <sup>a</sup> indicates unindexed additional weak lines. <sup>b</sup> indicates  $11\ell$  reflections of a  $3R$ -type additional phase

**Table 6.** Optimum structural parameters (atomic positions and occupancies) used for the simulation of sample KBi<sub>10h</sub> with 2*H* and 2*O* polytypes.

	2 <i>H</i> polytype				2 <i>O</i> polytype			
	<i>x</i>	<i>y</i>	$\zeta$ (Å)	Occ.	<i>x</i>	<i>y</i>	$\zeta$ (Å)	Occ.
Mn <sub>layer</sub>	0	0	0	0.98	0	0	0	0.98
O <sub>layer</sub>	±0.333	0	±1.000	2.00	±0.341	0	±1.000	2.00
K	-0.220	0	3.560	0.09	-0.250	0	3.560	0.09
K	0.110	±0.330	3.560	0.18	0.125	±0.375	3.560	0.18
H <sub>2</sub> O	0.150	0	3.560	0.17	0.150	0	3.560	0.53
H <sub>2</sub> O	0.075	±0.225	3.560	0.34	-	-	-	-

*Note:* Parameters defining the layer cation composition. Optimal values were determined by trial-and-error fitting of KBi<sub>10h</sub> experimental pattern (Figure 6d). *x* and *y* coordinates are expressed as fractions of the orthogonal *a* and *b* parameters, respectively. Coordinates along the *c*\* axis,  $\zeta$ , are expressed in Å to emphasize the thickness of layer and interlayer polyhedra.  $a = b\sqrt{3} = 4.976$  Å,  $b = 2.873$  Å (2*H* polytype – *P6<sub>3</sub>/mmc* space group),  $a_1 = 5.124$  Å,  $b_1 = 2.846$  Å,  $a_2 = 5.101$  Å,  $b_2 = 2.850$  Å, and  $a_3 = 5.084$  Å,  $b_3 = 2.853$  Å for the three 2*O* polytypes (*Cmcm* space group).  $c = 14.240$  Å,  $\alpha = \beta = \gamma = 90^\circ$  for all 4 phases. Debye-Waller factors were 0.5, 1.0, 2.0, 2.0 for Mn<sub>layer</sub>, O<sub>layer</sub>, K and H<sub>2</sub>O, respectively. Occupancies are given for the sum of all symmetrical sites. For all elementary contributions, the radius of the coherent scattering domains in the *ab* plane is 350 Å, whereas the mean coherent scattering domain along the *c*\* axis is 17 layers. All elementary contributions are devoid of random stacking faults.

**Table 7.** Selected inter-atomic distances calculated from the optimal atomic coordinates for KBi samples.

	<b>KBi<sub>10h</sub></b>				<b>KBi<sub>8h</sub> and KBi<sub>7</sub></b>		
	<i>2O-1</i>	<i>2O-2</i>	<i>2O-3</i>	<i>2H</i>	<i>2O</i>	<i>2H</i>	<i>3R</i>
Height of Mn layer	2.00	2.00	2.000	2.000	2.000	2.000	2.000
Mn <sub>layer</sub> -Mn <sub>layer</sub>	2.846 x2 2.931 x4	2.850 x2 2.922 x4	2.853 x2 2.915 x4	2.873 x6	2.855 x2 2.905 x4	2.855 x6	2.855 x6
Average Mn <sub>layer</sub> - Mn <sub>layer</sub>	2.903	2.898	2.894	2.873	2.888	2.855	2.855
Mn <sub>layer</sub> -O <sub>layer</sub>	1.929 x4 2.023 x2	1.929 x4 2.016 x2	1.929 x4 2.011 x2	1.946 x6	1.927 x4 2.003 x2	1.940 x6	1.938 x6
Average Mn <sub>layer</sub> - O <sub>layer</sub>	1.960	1.958	1.956	1.946	1.952	1.940	1.938
Mn <sup>3+</sup> <sub>interlayer</sub> -Mn <sub>layer</sub>	-	-	-	-	-	3.512	3.509
Mn <sup>3+</sup> <sub>interlayer</sub> -O <sub>layer</sub>	-	-	-	-	-	1.940	1.938
Mn <sup>3+</sup> <sub>interlayer</sub> - H <sub>2</sub> O <sub>interlayer</sub>	-	-	-	-	-	2.251	2.248
O <sub>layer</sub> -H <sub>2</sub> O <sub>interlayer</sub>	-	-	-	-	-	3.043	3.037
K <sub>interlayer</sub> -O <sub>layer</sub>	2.951 x2 3.295 x1	2.952 x2 3.289 x1	2.952 x2 3.284 x1	2.933 x2 3.377 x1	2.929 x2 3.373 x1	2.933 x2 3.444 x1	2.927 x2 3.439 x1
Average K <sub>interlayer</sub> - O <sub>layer</sub>	3.066	3.064	3.063	3.081	3.077	3.103	3.098
K <sub>interlayer</sub> - H <sub>2</sub> O <sub>interlayer</sub>	3.074 x1 3.507 x2	3.061 x1 3.505 x2	3.050 x1 3.504 x2	2.731 x2 3.135 x1 3.305 x1 3.412 x2	3.188 x1 3.414 x2	2.731 x2 3.223 x2 3.440 x2	2.731 x2 3.223 x2 3.440 x2
O <sub>layer</sub> -H <sub>2</sub> O <sub>interlayer</sub>	2.725	2.723	2.722	2.702	-	2.730	2.723
Note: All distances are given in Å.							

**Table 8.** Optimum structural parameters (atomic positions and occupancies) used for the simulation of sample KBi<sub>8h</sub> and KBi<sub>7</sub> with *2H*, *2O*, and *3R* polytypes.

	<b>2H polytype</b>				<b>2O polytype</b>				<b>3R polytype</b>			
	<b>x</b>	<b>y</b>	<b>ζ(Å)</b>	<b>Occ.</b>	<b>x</b>	<b>y</b>	<b>ζ(Å)</b>	<b>Occ.</b>	<b>x</b>	<b>y</b>	<b>ζ(Å)</b>	<b>Occ.</b>
Mn <sub>layer</sub>	0	0	0	0.85	0	0	0	0.98	0	0	0	0.85
O <sub>layer</sub>	±0.333	0	±1.000	2.00	±0.341	0	±1.000	2.00	±0.333	0	±1.000	2.00
Mn <sub>interlayer</sub>	0	0	±2.100	0.11	-	-	-	-	0	0	±2.100	0.11
H <sub>2</sub> O <sub>inter.</sub>	-0.333	0	3.580	0.33	-	-	-	-	-0.333	0	3.570	0.33
K <sub>inter.</sub>	-0.200	0	3.580	0.09	-0.220	0	3.550	0.09	-0.200	0	3.570	0.045
K <sub>inter.</sub>	0.100	±0.300	3.580	0.18	0.110	±0.330	3.550	0.18	0.100	±0.300	3.570	0.09
K <sub>inter.</sub>									-0.533	0	3.570	0.045
K <sub>inter.</sub>									-0.233	±0.300	3.570	0.09
H <sub>2</sub> O <sub>inter.</sub>	0.140	0	3.580	0.12	0.150	0	3.550	0.54	0.140	0	3.570	0.06
H <sub>2</sub> O <sub>inter.</sub>	-0.070	±0.210	3.580	0.24					-0.070	±0.210	3.570	0.12
H <sub>2</sub> O <sub>inter.</sub>									-0.193	0	3.570	0.06
H <sub>2</sub> O <sub>inter.</sub>									-0.263	±0.210	3.570	0.12

*Note:* Parameters defining the layer cation composition. Optimal values were determined by trial-and-error fitting of KBi<sub>8h</sub> and KBi<sub>7</sub> experimental pattern (Figures 9a, 10a). All notations as in Table 6. Debye-Waller factors are 0.5, 1.0, 1.5, 2.0, and 2.0 for Mn<sub>layer</sub>, O<sub>layer</sub>, Mn<sub>interlayer</sub>, K and H<sub>2</sub>O respectively. Occupancies are given for the sum of all symmetrical sites. For all elementary contributions, the radius of the coherent scattering domains in the *ab* plane is 350 Å (300 Å for the *2H/3R* MLS with a high *2H* content), whereas the mean coherent scattering domain along the *c*\* axis is 15 layers (20 layers for the *2O/2H* MLS). All elementary contributions are devoid of random stacking faults.



**Table 9.** Unit-cell parameters of the elementary  $2O$ ,  $2H$ , and  $3R$  polytypes present in KBi samples.

		KBi <sub>8h</sub> KBi <sub>7</sub>	KBi <sub>8o</sub> <sup>a</sup>		KBi <sub>10h</sub>		KBi <sub>10o</sub> <sup>b</sup>
$2O$	$a$	5.060	-	5.124	5.101	5.084	5.155
	$b$	2.855	-	2.846	2.850	2.853	2.846
	$a/b$	1.772	-	1.800	1.790	1.782	1.811
	$c$	14.220	-		14.240		14.088
$2H$	$a$	4.945	4.928		4.976		-
	$b$	2.855	2.845		2.873		-
	$a/b$	1.732	1.732		1.732		-
	$c$	14.320	14.235		14.240		-
$3R$	$a$	4.945	-		-		-
	$b$	2.855	-		-		-
	$a/b$	1.732	-		-		-
	$c$	21.420	-		-		-

*Note:* All unit-cell parameters are given in Å.  $\alpha = \beta = \gamma = 90^\circ$  for all phases. <sup>a</sup> Sample described by Gaillot et al.<sup>24</sup> <sup>b</sup> Sample described by Gaillot et al.<sup>25</sup>

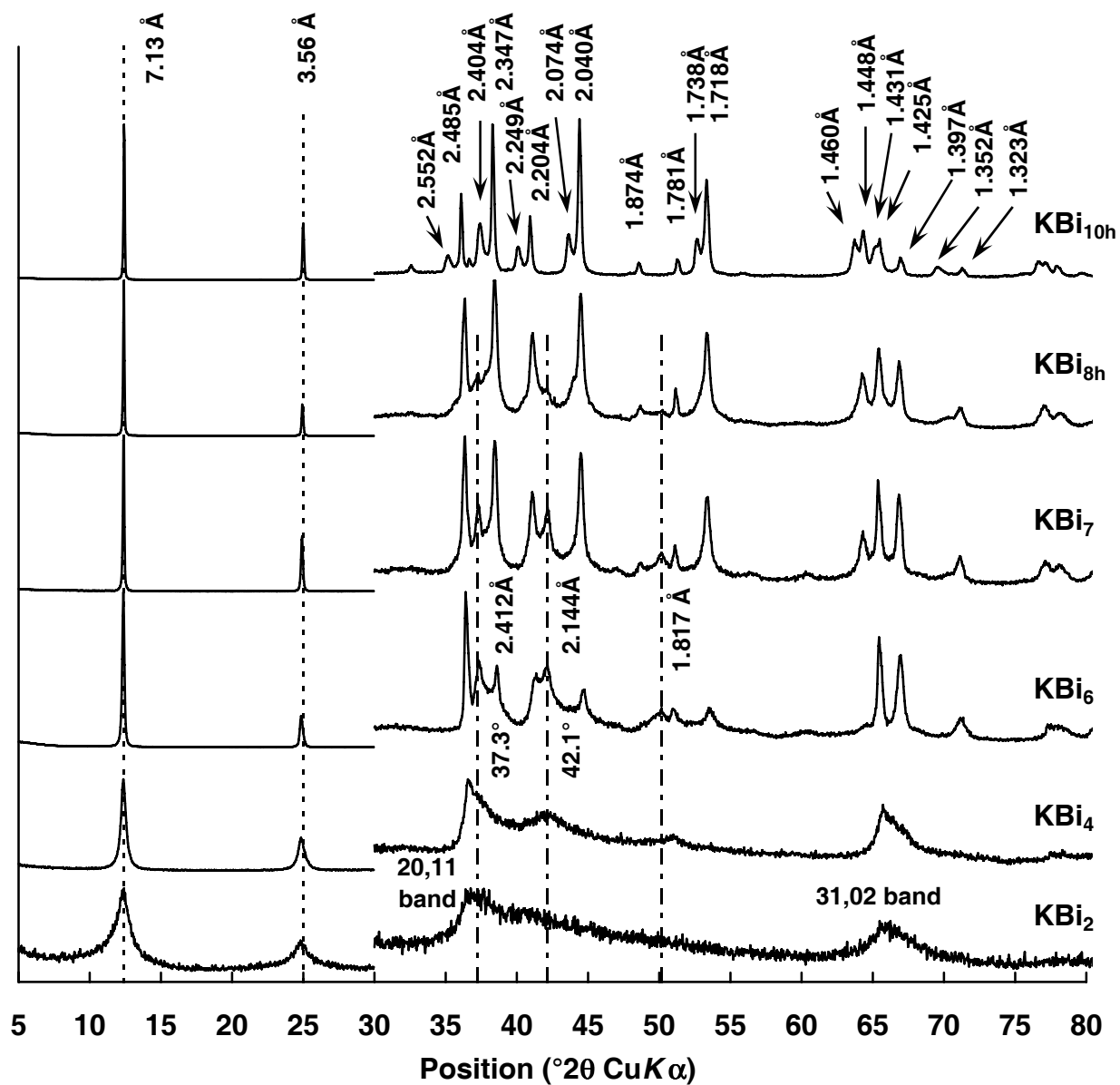
		350-KBi <sub>8h</sub>	350-KBi <sub>10h</sub>	350-KBi <sub>10o</sub> <sup>c</sup>
$2H$	$a$	4.980	5.013	5.014
	$b$	2.875	2.894	2.895
	$a/b$	1.732	1.732	1.732
	$c$	12.995	12.920	12.848

*Note:* All unit-cell parameters are given in Å.  $\alpha = \beta = \gamma = 90^\circ$  for all phases. <sup>c</sup> Sample described by Gaillot et al.<sup>25</sup>

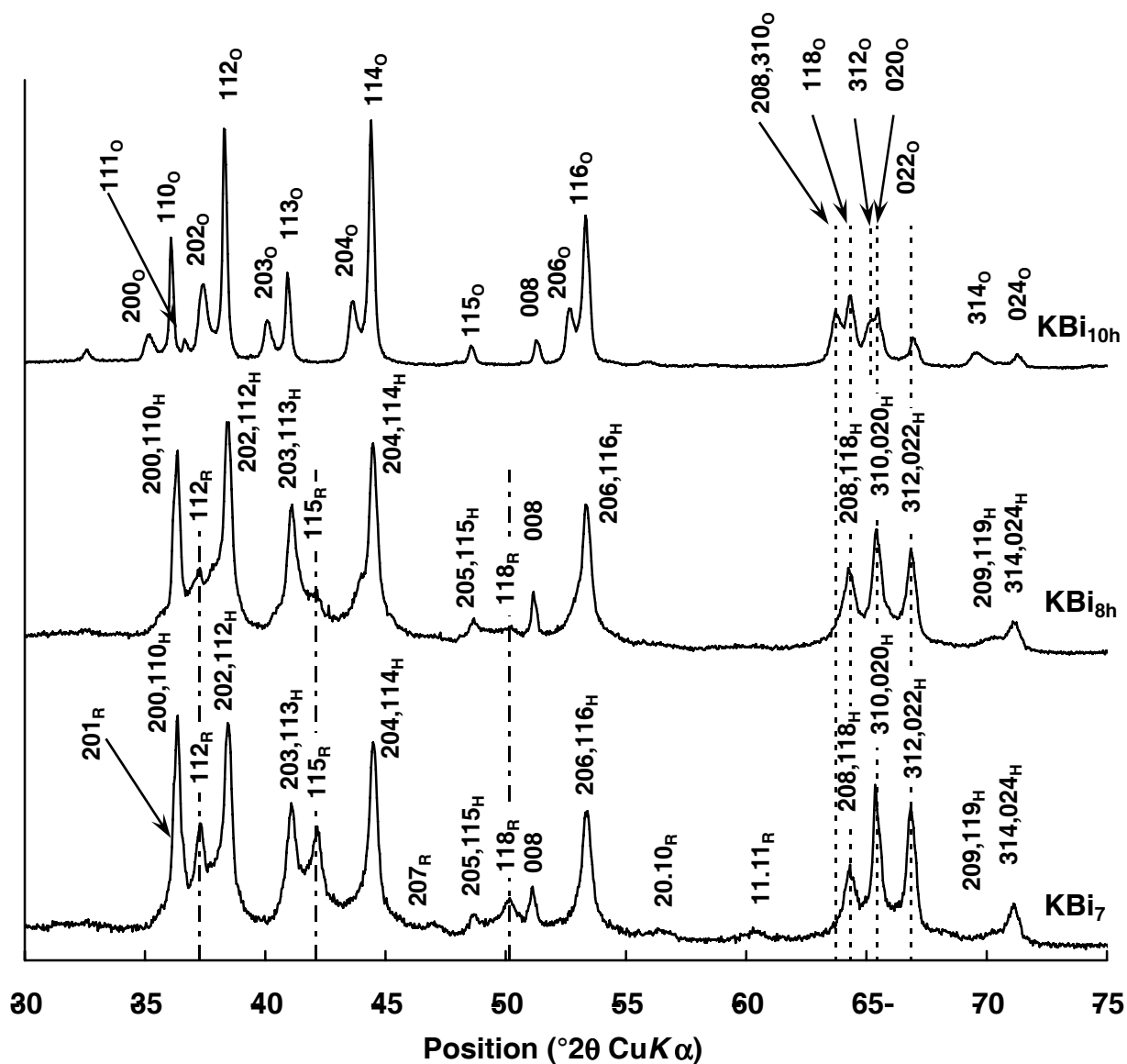
**Table 10.** Composition of the different elementary phases present in KBi samples.

	<i>3R/2H</i>		<i>2H/3R</i>		<i>2H</i>	<i>2O/2H</i>		<i>2O</i>	Total	
KBi <sub>7</sub>	23%		41%		7%	29%		-		
	<i>3R</i>	<i>2H</i>	<i>3R</i>	<i>2H</i>	<i>2H</i>	<i>2H</i>	<i>2O</i>	-	<i>2O</i>	15%
	90%	10%	30%	70%	100%	50%	50%	-	<i>2H</i>	53%
	21%	2%	12%	29%	7%	15%	15%	-	<i>3R</i>	33%
KBi <sub>8h</sub>	8%		48%		9%	34%		-		
	<i>3R</i>	<i>2H</i>	<i>3R</i>	<i>2H</i>	<i>2H</i>	<i>2H</i>	<i>2O</i>	-	<i>2O</i>	20%
	85%	15%	25%	75%	100%	40%	60%	-	<i>2H</i>	60%
	7%	1%	12%	36%	9%	14%	20%	-	<i>3R</i>	19%
KBi <sub>10h</sub>	-		-		24%	-		76%		
	-	-	-	-	<i>2H</i>	-	-	<i>2O</i>	<i>2O</i>	76%
	-	-	-	-	100%	-	-	100%	<i>2H</i>	24%
	-	-	-	-	24%	-	-	76%	<i>3R</i>	0%

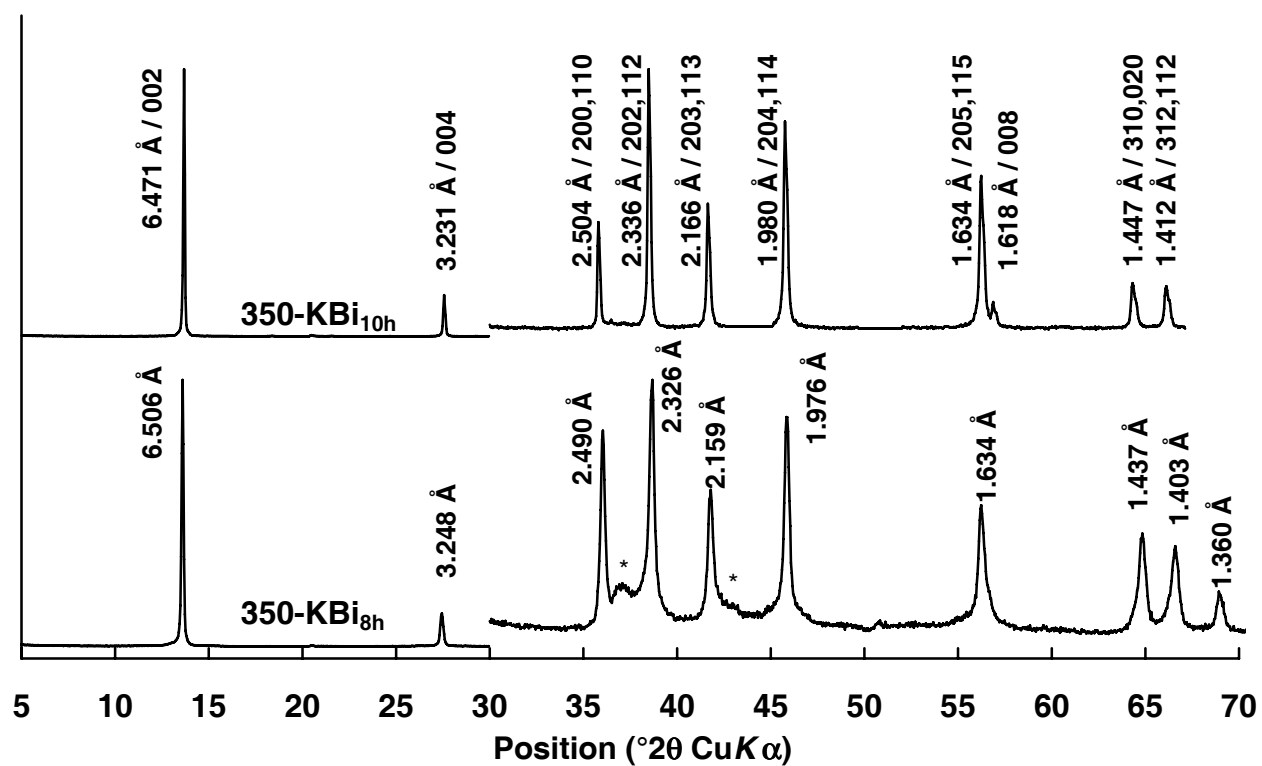
*Note:* For KBi<sub>10h</sub>, all contributions from *2O* polytypes with different unit cell parameters are all summed up.



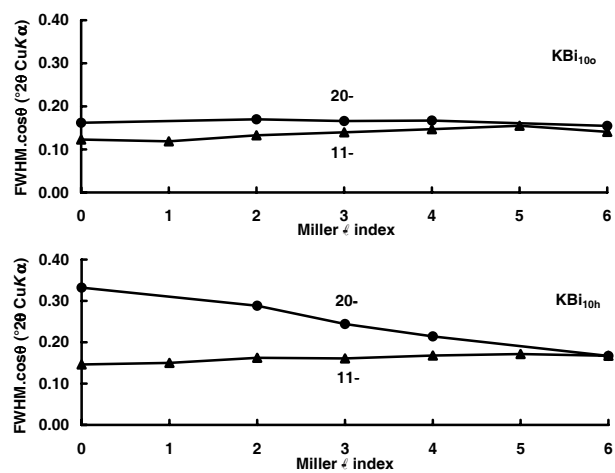
Please print in two column format



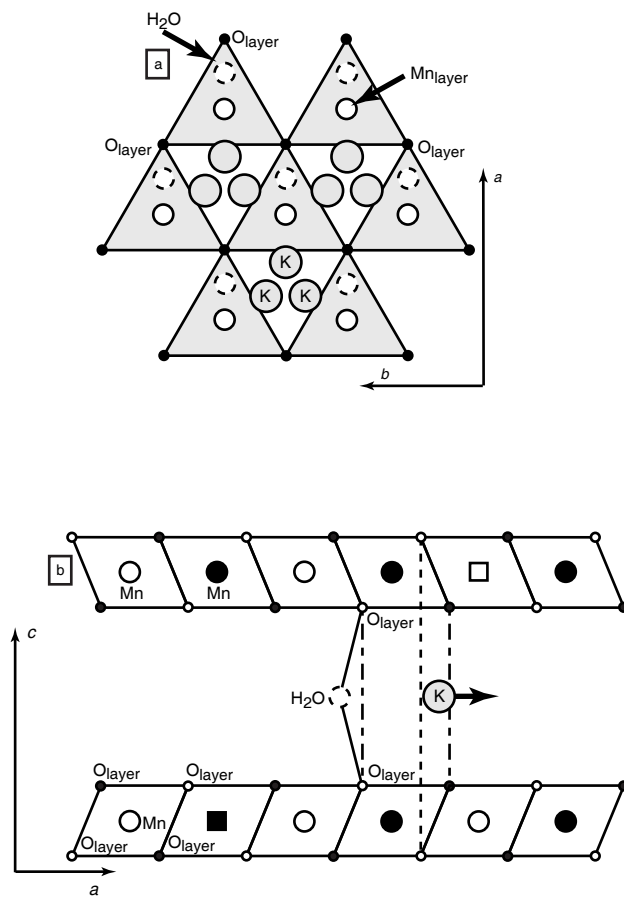
Please print in two column format



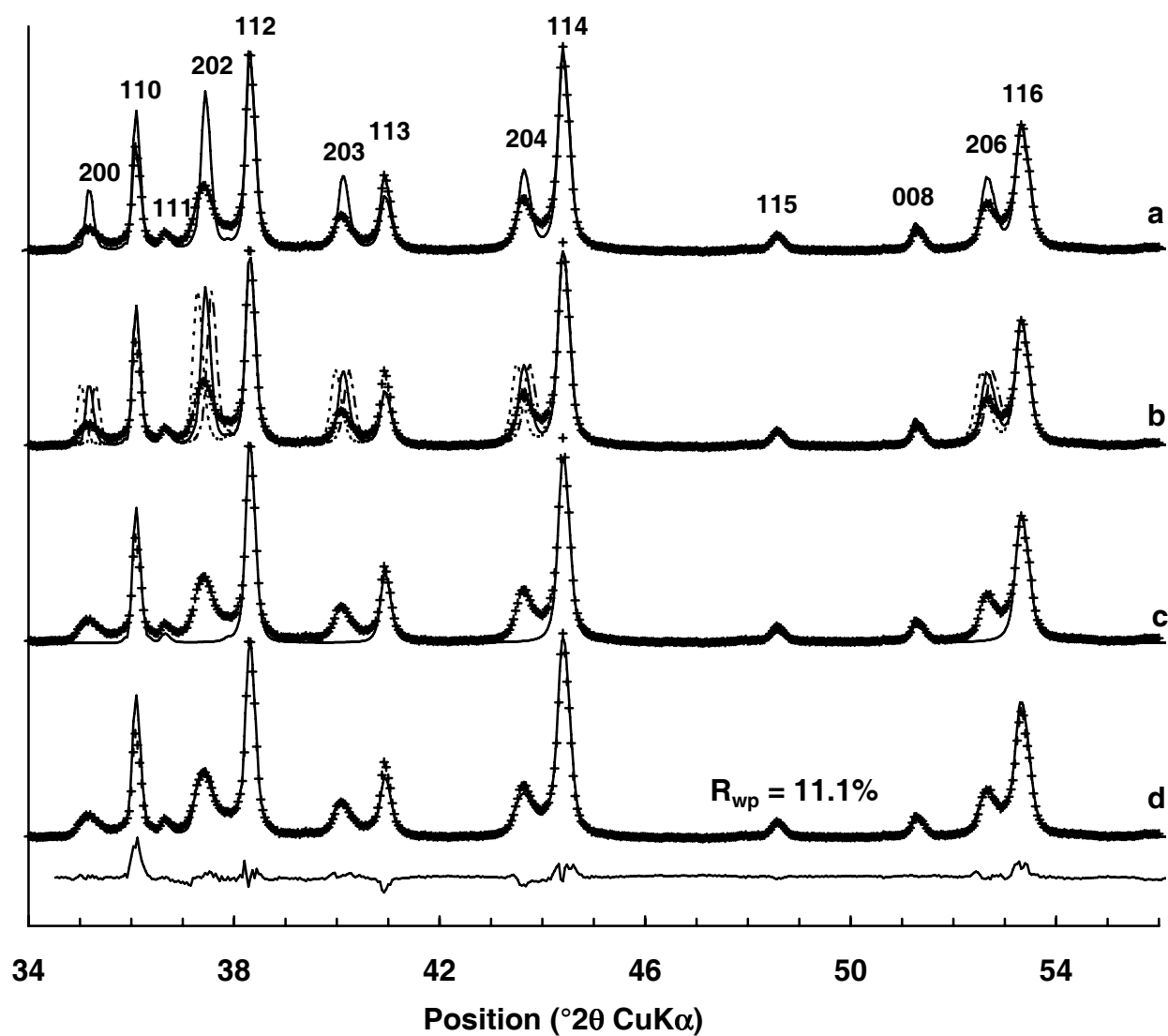
Please print in two column format



Please print in one column format

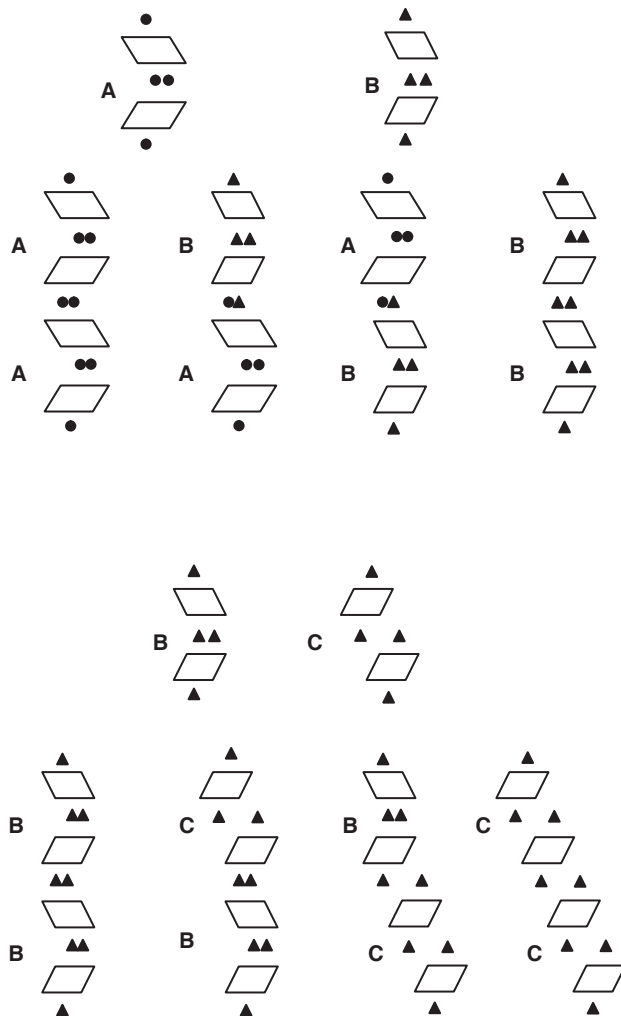


Please print in one column format

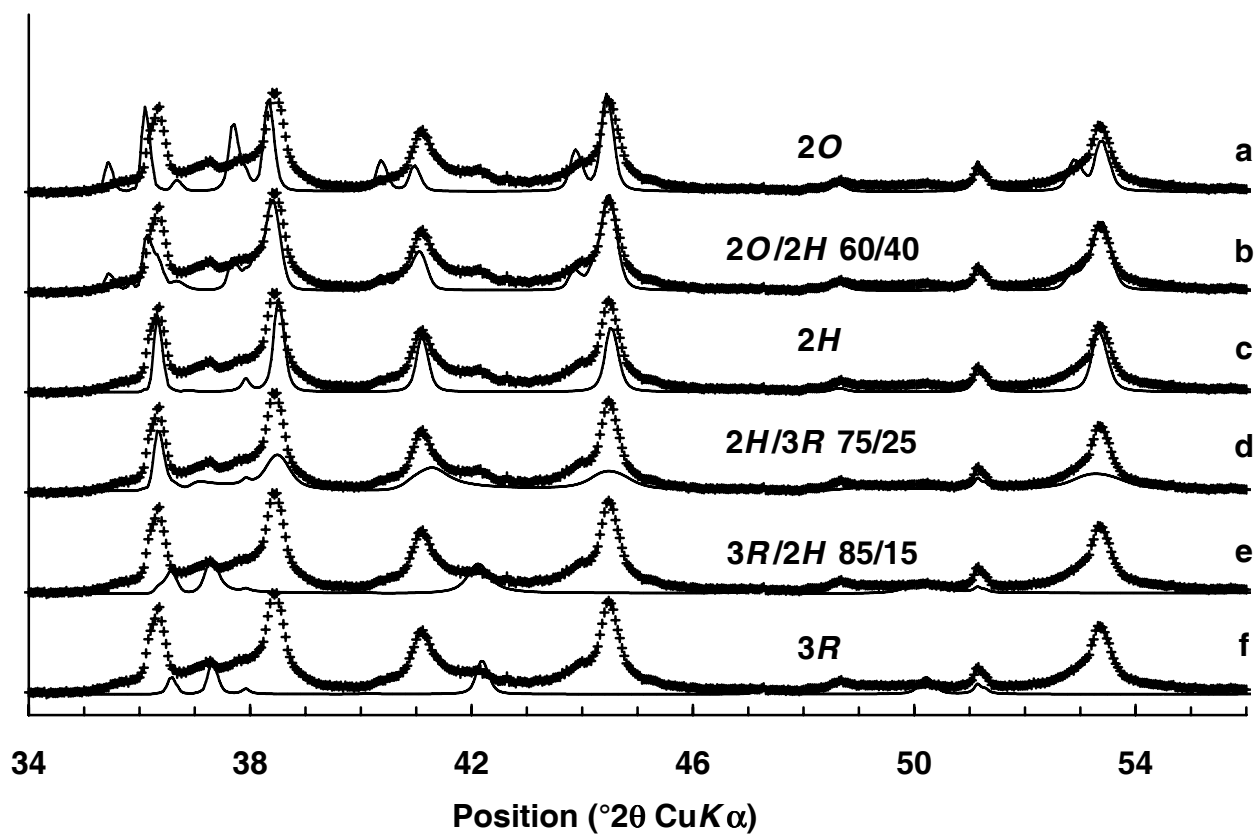


Please print in two column format

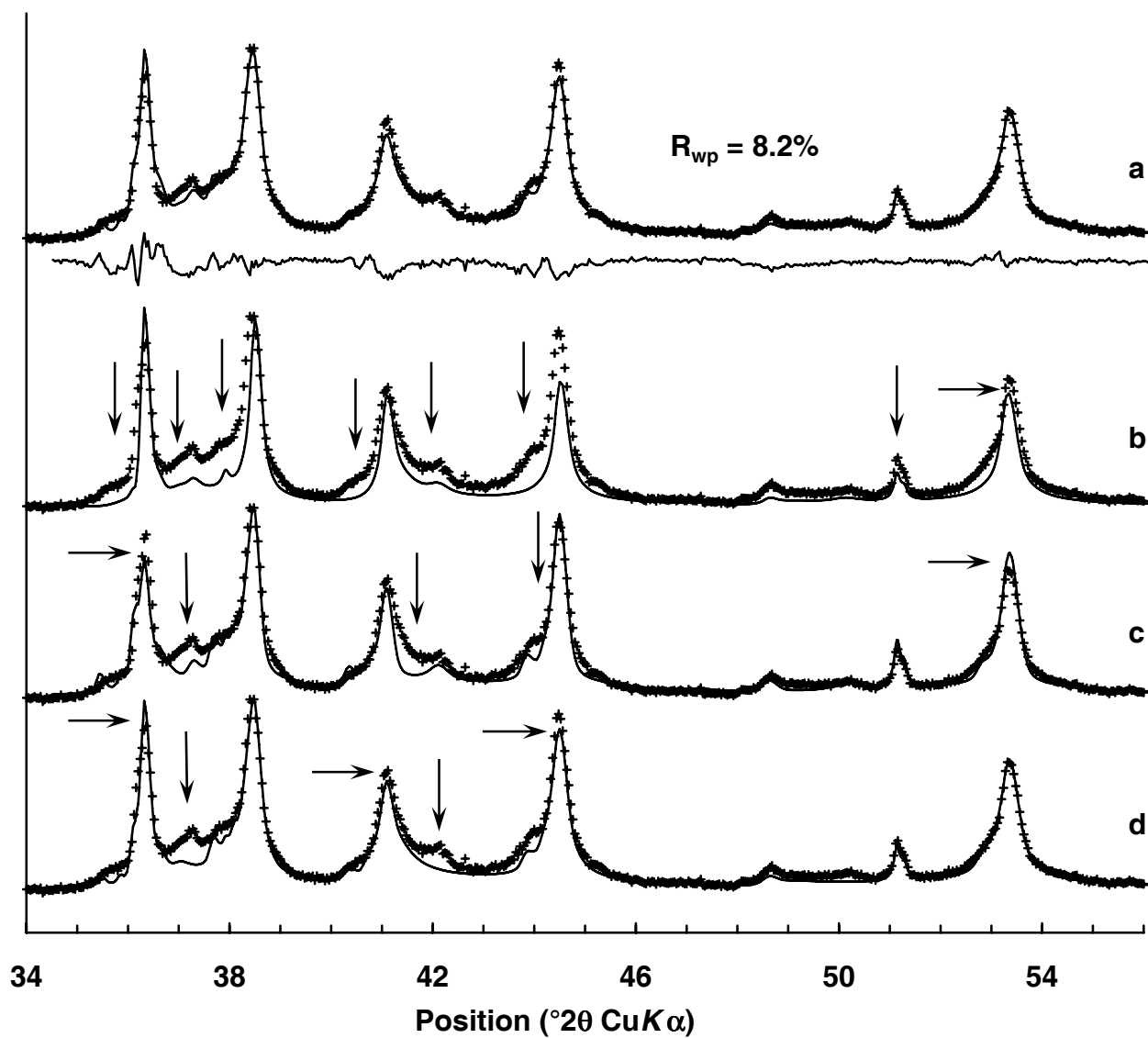




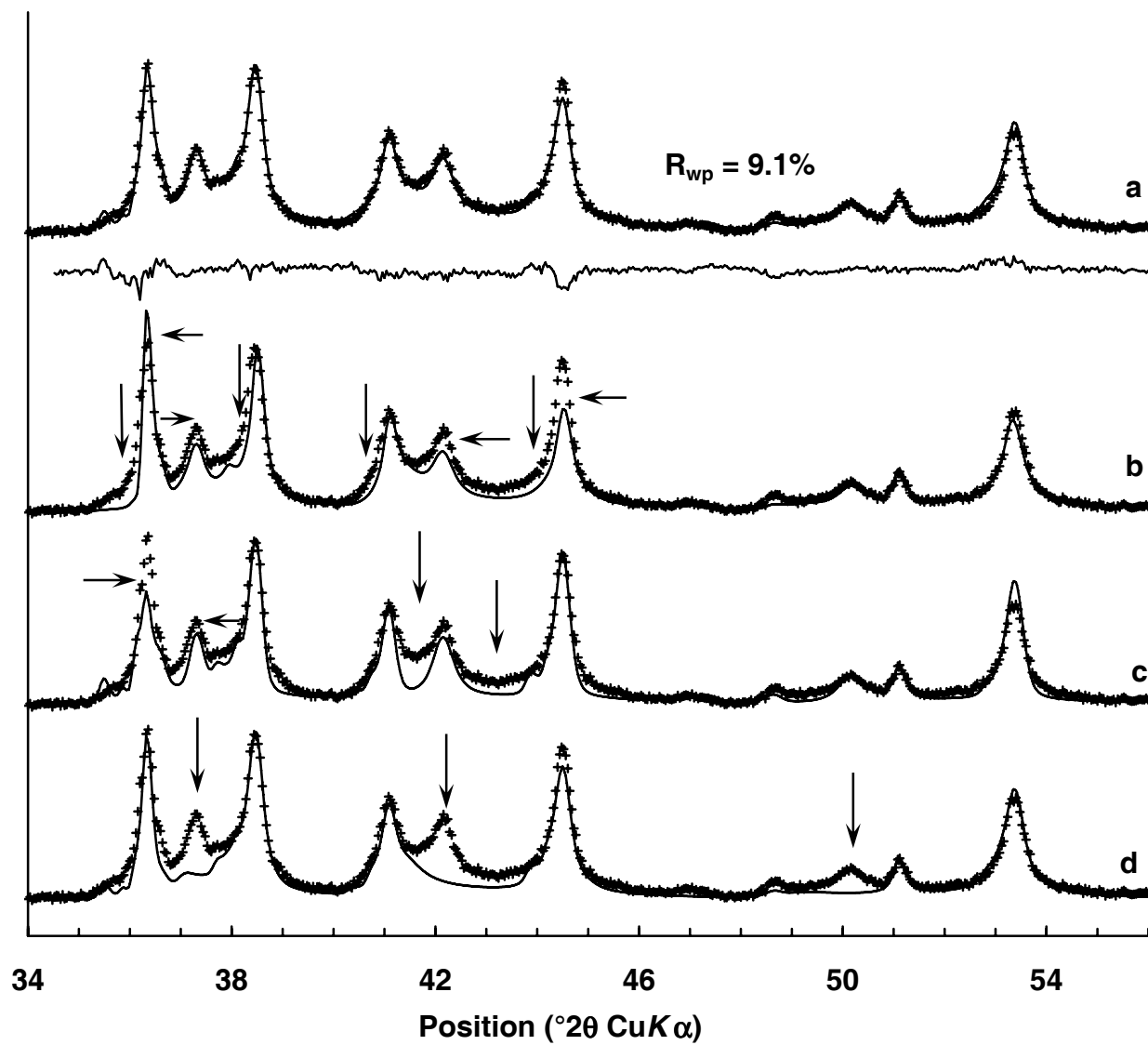
Please print in one column format



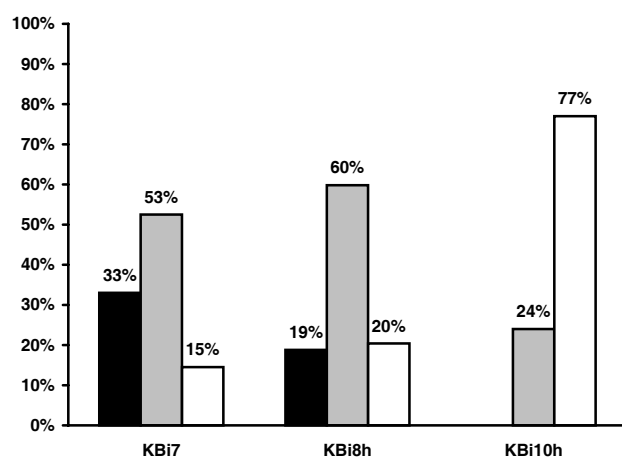
Please print in two column format



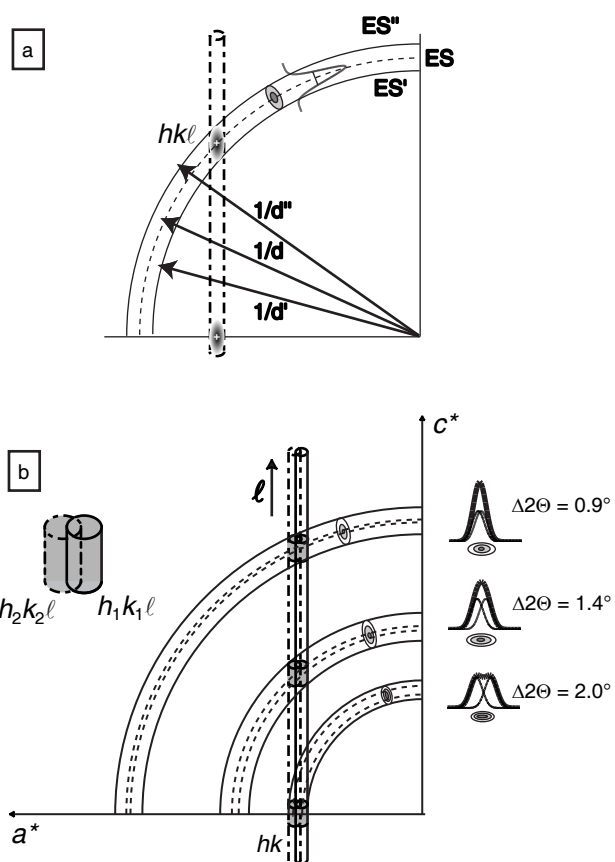
Please print in two column format



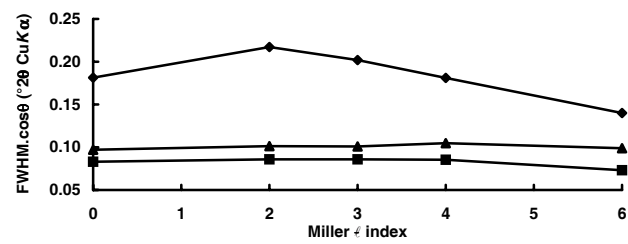
Please print in two column format



Please print in one column format



Please print in one column format



Please print in one column format